Supporting Information

Directing Structural Transformation in Gold(I)–Carborane Nanoclusters to Unlock Ultrafast Hypergolic Ignition

Index:

1. **Experimental details……S1**
2. **Single Crystal Structure Data……S8**
3. **NMR data……S42**
4. **Other data……S57**
5. **Rrferences……S66**

1. Experimental details

1.1 Materials and Equipment

All reagents and solvents were purchased from commercial sources and used as supplied unless otherwise specified. High resolution ESI-TOF-MS were recorded on an AB SCIEX TOFTOF 5800 in positive reflection mode. A few drops of HCOOH were added into Au_8 samples in order to enhance the signal intensities of neutral clusters. Both NMR and single crystal data were collected at *Center of Analytical Facilities of Nanjing University of Science and Technology*. NMR spectra were recorded on Bruker AVANCE III 500MHz and Bruker AVANCE NEO 500MHz. Spectra were recorded at room temperature unless otherwise specified. ^{1}H NMR spectra were recorded with chemical shifts (δ, ppm) relative to tetramethylsilane (Me_4Si). ^{31}P NMR spectra were recorded with chemical shifts (δ, ppm) relative to 85% H_3PO_4. Proton chemical shift (δ H = 7.26 ($CDCl_3$); 1.98 (CD_3CN); ppm) are reported relative to the solvent residual peak. Single crystal data were collected at low-temperature or room temperature by Cu or Mo target with the Bruker D8 Venture, single crystal instrument. UV-Vis absorption spectra were recorded on a Shimadzu UV-2600i Plus spectrophotometer. Solid-state emission spectra were acquired by an Edinburgh Instruments FLS 1000 spectrophotometer. X-ray photoelectron spectra (XPS) were acquired on a Thermo ESCALAB 250 with Al Kα ($h\nu$ = 1486.6 eV) as the excitation source. The constant-volume combustion energies of the compounds were determined by a precise oxygen bomb calorimetry (ZDHW-8000C).

1.2 Theoretical Calculations

The Gaussian 16 software was employed to perform calculations using the PBE1PBE functional and the def2-SVP basis set to optimize the ground state geometries [1]. The implicit solvent model was also considered, with

dichloromethane selected. The visualization of the orbitals was performed by GaussView 6.0 software [2].

1.3 Sensitive Test

The sensitivities of the compounds were determined according to the BAM (German: Bundesanstalt für Materialforschung und Prüfung) standard for friction and impact.

Impact sensitivity: The impact sensitivities of were tested on a BAM fall hammer produced by OZM Research Impact sensitivity tests according to STANAG 4489. A 5 kg weight was dropped from a set height onto a 10 mg sample placed on a copper cap. The test results showed that the explosion happened with approximate 50% initiation probability.

Friction sensitivity: The friction sensitivity was determined using a FSKM-10 BAM friction apparatus produced by OZM Research on the basis of STANAG 4487.

1.4 Droplet Test

A single drop of oxidant (white fuming nitric acid, WFNA) was added to a clear bottle using the “oxidant to fuel” droplet addition method. The oxidizer droplet's size was probably 20 μL with 10 mg samples. All ignition experiments carried out under ambient conditions were recorded using a high-speed camera running at 2000 frames per second. The time interval between the first contact of the oxidizer droplet with the fuel compound and the appearance of the flame was counted as the ignition delay time. Flame temperature was also captured, and analyzed by IRBIS professional software.

1.5 Synthesis and characterization

The synthesis routes of ligands such as 1,7-Bis(diphenylphosphine)carborane (*m*-P^P) [3], 1,2-Bis(diphenylphosphine)carborane (*o*-P^P) [4], were referred to the previous report with minor modifications. The overview synthesis routes can be seen as **Scheme S1**. Chromatography was performed on SepaBean machine SantaiTechnology Inc., China).

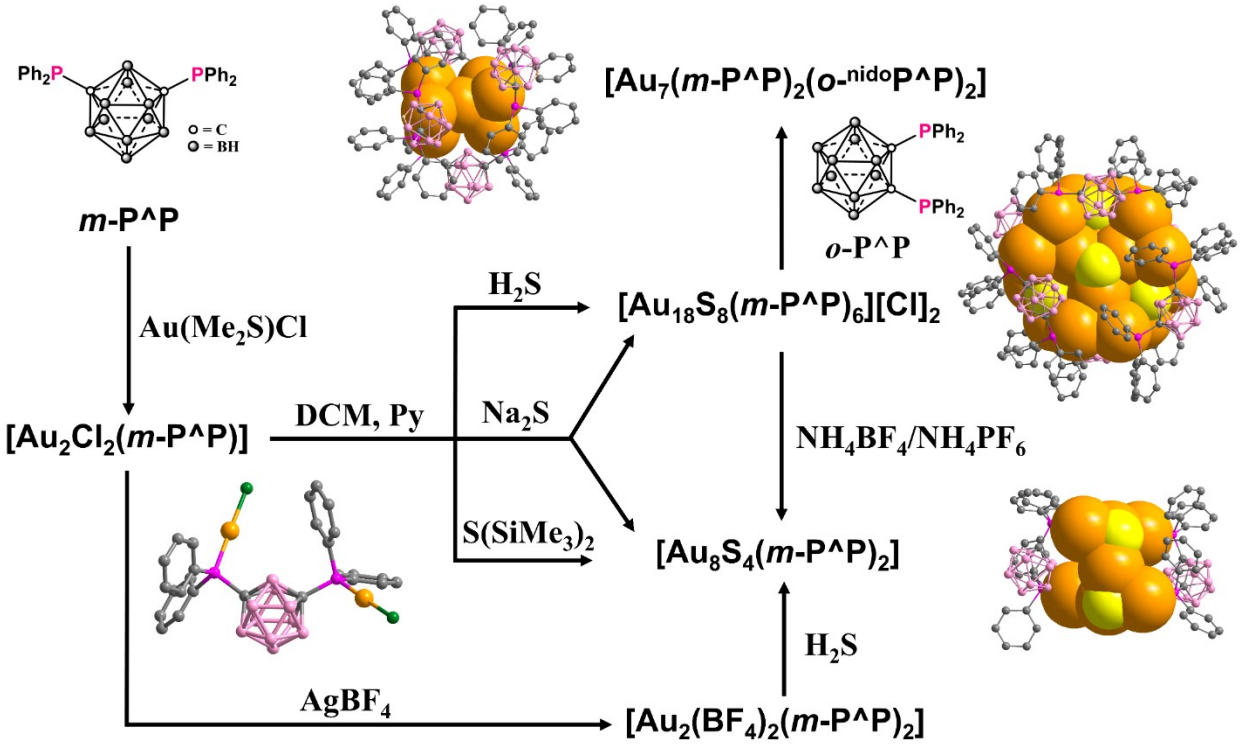

Scheme S1. Schematic diagram of synthesis routes.

Synthesis of 1,7-Bis(diphenylphosphine)carborane (***m*-P^P**): Generally, 1.6 mL of 1.6 mol/L *n*-BuLi (in hexane) (2.56 mmol, 2.56 equiv) was added to a Schlenk tube which con tained a solution of 144.2 mg of *m*-carborane (1.0 mmol, 1.0 equiv) in 10 mL of anhydrous Et_2O at 195 K over a period of 1 h with continuous stirring, then the Dewar Flask was removed and the stirring was continued at room temperature for another 1 h. 400 μL PPh_2Cl (slightly excess) was then added and the resulting mixture was stirred overnight. The reaction was quenched with water. The

organic phases were collected, and water phases were extracted by dichloromethane for three times. Anhydrous $NaSO_4$ was used to remove a small amount of water in organic phases. Then the reaction mixture was transferred to a flask and the organic phases was removed under vacuo to obtain oily residue. Column chromatography was employed to purify the crude product by using petroleum ether:ethyl acetate (5:1, *v*/*v*) as the eluent. Solvent removal and drying under vacuum resulted in 1,7-Bis(diphenylphosphine)carborane (*m*-P^P) as a white solid. Yield: 148 mg, 29%. ^{1}H NMR (500 MHz; $CDCl_3$, δ/ppm, 298K) δ = 7.55 (ddt, *J* = 8.7, 6.7, 1.6 Hz; 8H, Ph), 7.31–7.20 (m, 12H, Ph), 2.96–1.58 (br, 10H). ^{31}P{^{1}H} NMR (202 MHz, $CDCl_3$, δ/ppm): δ = 20.19.

Synthesis of [Au_2Cl_2(*m*-P^P)]: To a stirred solution of [Au(Me_2S)Cl] (0.1 mmol, 29.5 mg) in dichloromethane (10 mL) was added *m*-P^P (0.05 mmol, 25.3 mg) at room temperature. The mixture was stirred for 1 hour and the volume of the solution was concentrated under reduced pressure. Yield: 46 mg, 94%. Recrystallization by evaporating of acetonitrile solution yielded [Au_2Cl_2(*m*-P^P)] as prism transparent crystals. ^{1}H NMR (500 MHz, $CDCl_3$) δ = 8.04 – 7.96 (m, 8H, Ph), 7.68 – 7.54 (m, 12H, Ph). ^{31}P{^{1}H} NMR (202 MHz, $CDCl_3$, δ/ppm): δ = 57.11, ^{31}P{^{1}H} NMR (202 MHz, CD_3CN, δ/ppm): δ = 57.11.

Synthesis of crude [Au_2(*m*-P^P)$_2$][BF_4]$_2$ (with minor byproduct **[Au_2(*m*^{nido}-P^P)$_2$]):** To a solution of [Au_2Cl_2(*m*-P^P)] (0.02 mmol, 19.5 mg) in dichloromethane was added a solution of $AgBF_4$ (0.04 mmol, 7.8 mg) in CH_3OH, and then stirring for 10 min at dark place. This solution was centrifuged at 11000 rpm for 5 min to remove AgCl, and the volume of filter was concentrated under reduced pressure to obtain crude product [$Au_2(BF_4)_2$(*m*-P^P)$_2$]. ^{1}H NMR (500 MHz, $CDCl_3$) δ = 8.05 (dd, *J* = 14.0, 7.3 Hz, 8H), 7.73–7.61 (m, 12H). ^{31}P{^{1}H} NMR (202 MHz, $CDCl_3$, δ/ppm): δ

= 57.02. Positive MALDI-TOF-MS: *m/z*: simulated for $[Au_2C_{52}H_{60}B_{20}P_4]^{2+}$ ($[Au_2(m\text{-}P\text{^}P)_2]^{2+}$): 709.7468, experimental: 709.7451. By diffusion of *n*-hexane into dichloromethane solution, we failed to obtain the crystal of $[Au_2(m\text{-}P\text{^}P)_2][BF_4]_2$, but directly yielded several brown blcok crystals of byproduct $[Au_2(m\text{-}^{nido}P\text{^}P)_2]$. 57.50 ppm in ^{31}P NMR can be ascribed to this unexpected product.

Synthesis of 1,2-Bis(diphenylphosphine)carborane (***o*-P^P**): The synthesis routes of *o*-P^P is similar to *m*-P^P except that *m*-carborane was replaced by *o*-carborane. Column chromatography was employed to purify the crude product by using *n*-hexane: dichloromethane (8:2, *v*/*v*) as the eluent. Solvent removal and drying under vacuum resulted in *o*-P^P as a white solid. Yield: 134 mg, 26%. ^1H NMR (500 MHz, $CDCl_3$) δ = 7.76 (m, 8H, Ph), 7.36 (m, 12H, Ph). $^{31}P\{^1H\}$ NMR (202 MHz, $CDCl_3$, δ/ppm): δ = 7.31. 1-diphenylphosphine-carborane also can be isolated with yield of 36 mg.

Synthesis of $[Au_{18}S_8(m\text{-}P\text{^}P)_6][Cl]_2$ (Au_{18}): Freshly produced H_2S gas was bubbled into a solution of $[Au_2Cl_2(m\text{-}P\text{^}P)]$ (97.7 mg, 0.10 mmol) in dichloromethane-pyridine solution (30 ml) (5:1, v/v) at room temperature, resulting in a faint yellow solution gradually and further stirring 10 minutes. Then the reaction mixture was removed under rotary evaporation. Cyclohexane was added in the process of evaporation in order to remove high boiling points solution pyridine. By diffusion of *n*-hexane into dichloromethane solution yielded $[Au_{18}S_8(m\text{-}P\text{^}P)_6][Cl]_2$ as weak-yellow block crystals (*Z'* = 0.5 & 1.0). For powder sample, column chromatography was employed to purify by using DCM:CH_3OH (20:1, *v*/*v*) as the eluent. Yield: 61.4 mg, 53%. ^1H NMR (500 MHz, CD_3CN): δ = 8.74 (s, 2H, Ph), 8.56 – 7.34 (m, 18H, Ph). ^{31}P NMR (202 MHz, $CDCl_3$, 0.02 mg/μL, δ/ppm): δ = 50.21, $^{31}P\{^1H\}$ NMR (202 MHz, CD_3CN, 0.02 mg/μL, δ/ppm): δ = 50.24, ^{31}P NMR (202 MHz, CD_3OD,

0.02 mg/μL, δ/ppm): δ = 50.28. ^{31}P NMR (202 MHz, $CDCl_3$, 0.08 mg/μL, δ/ppm): δ = 51.71, 50.79, 50.22. Positive MALDI-TOF-MS: *m/z*: simulated for $[C_{156}H_{178}B_{60}P_{12}Au_{18}S_8]^{2+}$ ($[Au_{18}S_8(m\text{-P^P})_6]^{2+}$): 3437.9387, experimental: 3737.9360.

Synthesis of $[Au_8S_4(m\text{-P^P})_2]$ (Au_8)

Method 1: To a solution of $[Au_{18}S_8(m\text{-P^P})_6][Cl]_2$ in dichloromethane was added a saturated solution of NH_4BF_4 or NH_4PF_6 in saturated CH_3OH, respectively and stirring for 1 d. Low concentration of reaction materials can avoid white precipitates. Subsequent recrystallization by diffusion of *n*-hexane into above concentrated solution yielded weak-yellow block crystals of Au_8.

Method 2: The synthesis and single crystal growth procedure of **Au_8** was similar to that described for $[Au_{18}S_8(m\text{-P^P})_6][Cl]_2$ except $[Au_2Cl_2(m\text{-P^P})]$ was replaced by $[Au_2(m\text{-P^P})_2][BF_4]_2$. Namely, H_2S was bubbled into $[Au_2(m\text{-P^P})_2][BF_4]_2$ in DCM/pyridine solution (5:1, *v*/*v*). Subsequent recrystallization by diffusion of *n*-hexane into DCM solution.

Method 3: The procedure was similar to that described for $[Au_{18}S_8(m\text{-P^P})_6][Cl]_2$ except that H_2S was replaced by $S(SiMe_3)_2$. Subsequent recrystallization by diffusion of *n*-hexane into DCM solution.

^{1}H NMR (500 MHz, $CDCl_3$, δ/ppm): δ = 8.83–8.63 (br, 2H, Ph), 8.30–7.44 (m, 18H, Ph). ^{31}P{^{1}H} NMR (202 MHz, $CDCl_3$, δ/ppm): δ = 48.84. Extra HCOOH was added in the test of positive MALDI-TOF-MS. *m/z*: simulated for $[C_{52}H_{62}Au_8B_{20}P_4S_4]^+$ ($[Au_8S_4(m\text{-P^P})_2 + 2H]^+$): 2730.2010, experimental: 2730.2019.

Synthesis of $[Au_7(m\text{-P^P})_2(o\text{-}^{nido}P^P)_2]$ (Au_7, $o\text{-}^{nido}P^P$ = 7,8-Bis(diphenylphosphine)-nido-carborane): To a solution of $[Au_{18}S_8(m\text{-P^P})_6][Cl]_2$

in dichloromethane added *o*-P^P (~5 equ.) and stirring for 1 day. Subsequent recrystallization by diffusion of *n*-hexane into above solution yielded red-orange block crystals of Au_7. Yield: 21% (based on *m*-P^P). ^{1}H NMR (500 MHz, $CDCl_3$, δ/ppm): δ = –2.38 ~ –1.80 (s, 2H). ^{31}P NMR (202 MHz, $CDCl_3$, δ/ppm): δ = 95.80, 60.67, 60.01. Positive MALDI-TOF-MS: *m/z*: simulated for $[Au_2C_{52}H_{60}P_4B_{19}]^+$ ($[Au_2(m\text{-P^P})(o\text{-}^{nido}P^P)]^+$): 1408.4848, experimental: 1408.4864; $[Au_2C_{78}H_{90}P_6B_{29}]^+$ ($[Au_2(m\text{-P^P})_2(o\text{-}^{nido}P^P)]^+$): 1919.7710, experimental: 1919.7628.

2. Single Crystal Structure Data

2.1 Single Crystal Structure Determination and Alerts Response

In general, the current crystal diffraction data were collected at the *Center of Analytical Facilities of Nanjing University of Science and Technology*. The data was collected by D8 VENTURE equipping with Cu and Mo double X-ray source. The integration and absorption correction were all operated on APEX 6 SOFTWARE. All crystal data were solved with the olex2.solve [5] structure solution program using Charge Flipping and refined with the SHELXL [6] refinement package using Least Squares minimisation. All non-H atoms of the complexes were refined with anisotropic thermal parameters. The hydrogen atoms were included in idealized positions and refined with fixed geometry with respect to their carrier atoms.

The data quality of **[Au_2Cl_2(*m*-P^P)]** was satisfactory, no extra restrictions were added and no voids or solvent molecules were observed and further confirmed by Platon SOFTWARE.

For **[Au_2(*m*-^{nido}P^P)$_2$]**, the limited crystal quantity resulted in low I/σ ratios at high diffraction angle (>50°). *R* indexes are increasing rapidly as the I/σ values decreasing (R_1 = 0.0820, wR_2 = 0.1874 for I>=2σ (I); R_1 = 0.1607, wR_2 = 0.2607 for all data). Repeated attempts to select alternative crystals were unsuccessful. The weak diffraction intensity at high angles likely contributes to Alerts B of RINTA01, PLAT020, PLAT342. Regarding PLAT971_ALERT_2_A, the residual electron density peak is situated near atom B1 (distance: 1.11 Å) and does not correspond to any significant unassigned electron density. For PLAT973_ALERT_2_A and PLAT971_ALERT_2_B, the remaining Q peaks are localized around the heavy gold atoms, possibly due to imperfect absorption correction. One phenyl ring was modeled with disorder and split over two sites. The contribution of disordered solvent molecules was accounted for computationally using the PLATON/SQUEEZE program.

The *X*-ray diffraction data quality of nanoclusters is generally lower than that of typical coordination compounds, primarily due to aggregation-induced absorption effects from heavy atoms, which complicate absorption correction and frequently trigger CheckCIF Alerts such as PLAT971, PLAT972, and PLAT973. These alerts, commonly encountered in heavy-element cluster crystallography, are acknowledged but not considered to affect the structural conclusions, and are therefore ignored from the subsequent discussion.

MALDI-TOF-MS analysis of **$[Au_{18}S_8(m\text{-}P\text{^}P)_6][Cl]_2$** confirms the 2+ charged nature of the metal cluster, corresponding to the formulation $[C_{156}H_{178}B_{60}P_{12}Au_{18}S_8]^{2+}$. Throughout the synthetic pathway, no potential counter anions other than chlorine atoms were introduced, suggesting that Cl^- represents the only potential counterions co-crystallized within the lattice of the $[Au_{18}S_8(m\text{-}P\text{^}P)_6][Cl]_2$ nanocluster. In the case of $[Au_{18}S_8(m\text{-}P\text{^}P)_6][Cl]_2$ (Z' = 0.5), *X*-ray diffraction data were collected at 296.00 K. Attempts to improve data quality by collecting data at 100 K did not yield significant enhancements, and solvent molecules—including potential water molecules—remained difficult to model explicitly. Their electron density was therefore processed using the PLATON/SQUEEZE program, which indicated a solvent-accessible void volume of 530 Å³ containing approximately 86 electrons, though the exact solvent composition could not be confidently assigned. To improve the single crystal model, refinement constraints and restraints—including AFIX 66 and SIMU 0.01 0.02—were applied to optimize the geometry and displacement parameters of phenyl rings. Nevertheless, the low precision of C–C bond determinations resulted in CheckCIF Alert B (PLAT342_ALERT_3_B: Low Bond Precision on C–C Bonds ≈ 0.05486 Å). Additional A- and B-level alerts (e.g., THETM01, PLAT971, PLAT972, PLAT973) stem from disordered solvent molecules, substantial void spaces, and the characteristically strong absorption effects caused by heavy gold atom aggregation.

The calculated electron count in the void volume (2244 Å^3 with 625 electrons) was hard to determine solvent types and squeezed by PLATON/SQUEEZE program.

Fortuitously, we also obtained single crystals of $[Au_{18}S_8(m\text{-P^P})_6][Cl]_2$ with *Z'* = 1.0 from the same pot at 100.15 K. They (*Z'* = 0.5 and 1.0) both belong to the triclinic *P-1* space group. We initially hypothesized that temperature might cause the distinct stacking modes, but in situ variable-temperature single-crystal *X*-ray diffraction (100–300 K) showed negligible variation in unit cell volumes (11,320–10,837 Å^3), ruling out temperature as the origin of the structural differences. Unit cell screening of approximately 15 individual Au_{18} crystals at 100 K revealed that only three exhibited volumes around 11,000 Å^3, indicating the coexistence of two subtly distinct crystalline phases. Although both of them morphologies exhibit identical morphologies under the microscope—displaying faint yellow, almost colorless block crystals. Their slight structural distinction is discernible from the diffraction data. The single-crystal determination procedures and the resulting CheckCIF alerts for Au_{18} (*Z'* = 1.0) are closely parallel to those for Au_{18} (*Z'* = 0.5), and have therefore not been elaborated in detail.

To determine the final products, single-crystal *X*-ray diffraction data of **$[Au_8S_4(m\text{-P^P})_2]$** were collected *via* four distinct routes: (a) Au_{18} + NH_4BF_4, (b) Au_{18} + NH_4PF_6, (c) $[Au_2(m\text{-P^P})_2][BF_4]_2$ + H_2S and (d) $[Au_2Cl_2(m\text{-P^P})]$ + $S(SiMe_3)_2$ (Detailed unit cell parameters are listed in **Figure S1**). They all belong to *P2$_1$/c* space group with the same framework, and their cell parameters show minor differences. All A- and B-level Alerts have been resolved for crystal data (b) Au_{18} + NH_4PF_6. Thus, it represents the single crystal of Au_8 in the manuscript. For (a) Au_{18} + NH_4BF_4, one free CH_2Cl_2 solvent molecule could be determined; For (c) $[Au_2(m\text{-P^P})_2][BF_4]_2$ + H_2S, due to very low resolution (1.42 Å), B and C atoms are not carried out anisotropic refinement (PLAT201_ALERT_2_A), the position of B and C atoms are not decided well but the position of heavy atoms can determine.

Although there were limitations and difficulties encountered during data collection and absorption correction because of the limitation of the facility, the crystal instability, and the large number of highly disordered lattice solvent molecules, which hindered the establishment of the coordinates of the monoatomic counter-anions in the crystal lattice, with the supports from other characterization, the current model reveals the best possible structure of the cationic Au cluster, which is reasonable and consistent with other experimental findings such as MALDI-TOF-MS and NMR data.

2.2 Comparison of Au_8 crystals with different routes

we also compared the single-crystal structures of **Au_8** obtained *via* four different routes (**Figure S1** and **S3**). Surprisingly, although no buffer anions are present in the final **Au_8** structure, the average Au–Au bond lengths seem to be influenced by the anions. In systems derived from $[Au_2(m\text{-P}\hat{}\text{P})_2][BF_4]_2 + H_2S$ and $[Au_2Cl_2(m\text{-P}\hat{}\text{P})] + NH_4BF_4$, not only the average Au–Au bond lengths are very close (3.1128 and 3.1162 Å, respectively), but all twelve corresponding Au–Au bond distances also exhibit nearly identical values, respectively (**Figure S3**). In contrast, routes of $[Au_2Cl_2(m\text{-P}\hat{}\text{P})] + S(SiMe_3)_2$ and $[Au_2Cl_2(m\text{-P}\hat{}\text{P})] + NH_4PF_6$ yield average Au–Au bond lengths of 3.0797 and 3.0956 Å, respectively. The errors are much larger. Above results further support that BF_4^- ions may promote the structural transformation of $[Au_2(m\text{-P}\hat{}\text{P})_x]^{2+}$ (x = 1 or 2) to **Au_8**.

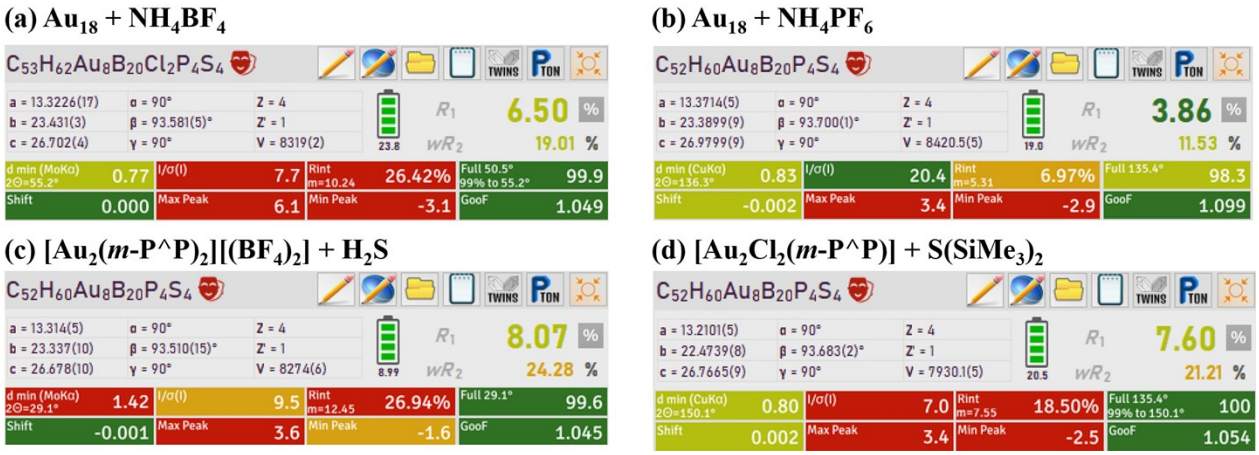

Figure S1. Detailed cell parameters of **Au_8** with different synthesizing strategies.

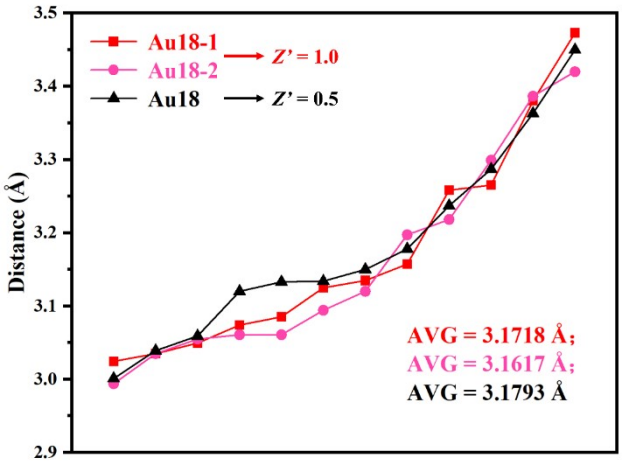

Figure S2. Au–Au bond distances in the **Au_{18}** Cluster (from shortest to longest). Au18-1 and Au18-2 represent two different cores in Au_{18} (***Z'* = 1.0, T = 100.00 K**) while Au18 represents the single core in **Au_{18}** (***Z'* = 0.5, T = 296.00 K**). Detailed parameters see **Table S2**.

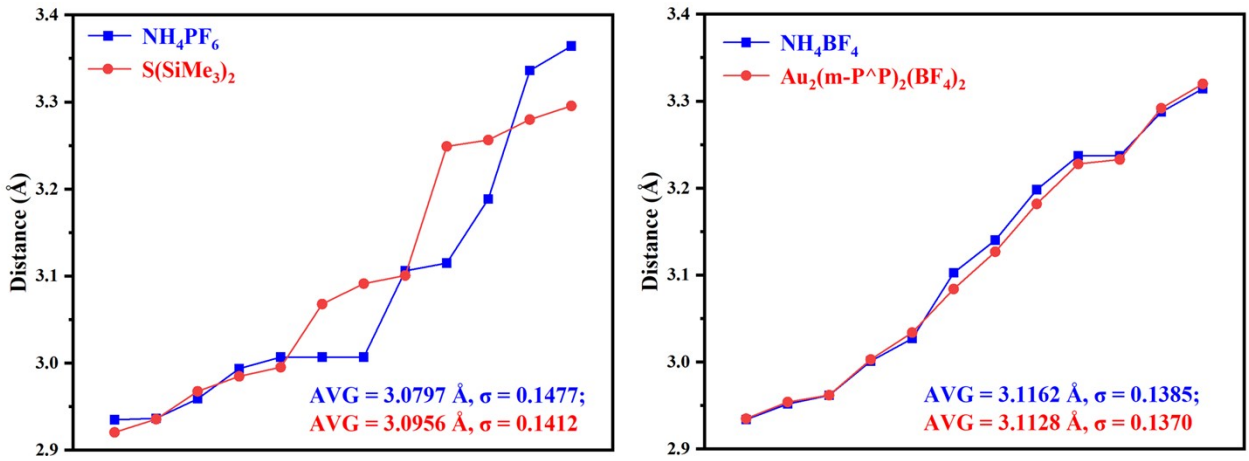

Figure S3. Au–Au Bond Distances in the Au_8 Clusters by employing different synthesis routes (from shortest to longest). All data are collected at 100.15 K. Detailed parameters see **Table S2**.

2.3 Refinement parameters

Table S1. Crystal data and structure refinement parameters

Compound	**[Au_2Cl_2(*m*-P^P)]**
CCDC	2454644
Radiation	CuKα (λ = 1.54184 Å)
Empirical formula	$C_{26}H_{30}Au_2B_{10}Cl_2P_2$
M_r *(g mol^{-1})*	977.37
Temperature/K	174.15
Crystal system	monoclinic
Space group	$P2_1/c$
a/Å	10.1696(3)
b/Å	23.2022(6)
c/Å	13.7961(4)
α/°	90
β/°	100.2800(10)
γ/°	90
Volume/Å^3	3203.03(16)
Z	4
D_c*/g cm^{-3}*	2.027
F (*000*)	1832.0
Reflections collected	26860
Independent reflections	5837 [R_{int} = 0.0429, R_{sigma} = 0.0350]
GOF on F^2	1.139
Final R indexes [I>=2σ (I)]	R_1 = 0.0341, wR_2 = 0.0869
Final R indexes [all data]	R_1 = 0.0378, wR_2 = 0.0879

$R_1 = \sum(F_o - F_c)/\sum F_o$; $wR_2 = [\sum w(F_o^2 - F_c^2)^2/\sum w(F_o^2)^2]^{1/2}$.

Compound	**$[Au_2(m\text{-}^{nido}P\text{^}P)_2]$**
CCDC	2495585
Radiation	MoKα (λ = 0.71073)
Empirical formula	$C_{52}H_{60}Au_2B_{18}P_4$
M_r *(g mol^{-1})*	2794.78
Temperature/K	100.15
Crystal system	monoclinic
Space group	*C2/c*
a/Å	25.395(3)
b/Å	11.2877(13)
c/Å	22.043(2)
α/°	90
β/°	98.439(4)
γ/°	9
Volume/Å^3	6250.2(12)
Z	4
D_c*/g cm^{-3}*	1.485
F (*000*)	2720.0
Reflections collected	68146
Independent reflections	7746 [R_{int} = 0.2234, R_{sigma} = 0.1242]
GOF on F^2	1.013
Final R indexes [I>=2σ (I)]	R_1 = 0.0820, wR_2 = 0.1874
Final R indexes [all data]	R_1 = 0.1607, wR_2 = 0.2607

$R_1 = \sum(F_o - F_c)/\sum F_o$; $wR_2 = [\sum w(F_o^2 - F_c^2)^2/\sum w(F_o^2)^2]^{1/2}$.

Compound	**$[Au_{18}S_8(m\text{-}P\text{^}P)_6][Cl]_2$ (Z' = 0.5)**
CCDC	2454647
Radiation	MoKα (λ = 0.71073 Å)
Empirical formula	$C_{156}H_{180}Au_{18}B_{60}Cl_2P_{12}S_8$
M_r *(g mol^{-1})*	6948.01
Temperature/K	296.00
Crystal system	triclinic
Space group	*P-1*
a/Å	17.012(5
b/Å	18.535(5)
c/Å	19.375(5)
α/°	101.561(6)
β/°	109.044(6)
γ/°	104.722(6)
Volume/Å^3	5310(2)
Z	1
D_c*/g cm^{-3}*	2.173
F (*000*)	3180.0
Reflections collected	82652
Independent reflections	11765 [R_{int} = 0.2264, R_{sigma} = 0.1486]
GOF on F^2	1.064
Final R indexes [I>=2σ (I)]	R_1 = 0.1128, wR_2 = 0.2630
Final R indexes [all data]	R_1 = 0.1790, wR_2 = 0.3391

$R_1 = \sum(F_o - F_c)/\sum F_o$; $wR_2 = [\sum w(F_o^2 - F_c^2)^2/\sum w(F_o^2)^2]^{1/2}$.

Compound	**$[Au_{18}S_8(m\text{-}P\text{^}P)_6][Cl]_2$ (Z' = 1.0)**
CCDC	2454645
Radiation	CuKα (λ = 1.54184 Å)
Empirical formula	$C_{156}H_{180}Au_{18}B_{60}Cl_2P_{12}S_8$
M_r *(g mol^{-1})*	6948.01
Temperature/K	100.00
Crystal system	triclinic
Space group	*P-1*
a/Å	19.8665(8)
b/Å	21.7317(9)
c/Å	27.7325(12)
α/°	94.188(2)
β/°	98.263(2)
γ/°	105.822(2)
Volume/Å^3	11320.4(8)
Z	2
D_c*/g cm^{-3}*	2.038
F (*000*)	3180.0
Reflections collected	151725
Independent reflections	44694 [R_{int} = 0.0813, R_{sigma} = 0.0882]
GOF on F^2	1.097
Final R indexes [I>=2σ (I)]	R_1 = 0.0946, wR_2 = 0.2633
Final R indexes [all data]	R_1 = 0.1270, wR_2 = 0.2808

$R_1 = \sum(F_o - F_c)/\sum F_o$; $wR_2 = [\sum w(F_o^2 - F_c^2)^2/\sum w(F_o^2)^2]^{1/2}$.

Compound	**$[Au_8S_4(m\text{-}P\hat{}P)_2]$ (a) $Au_{18} + NH_4BF_4$**
CCDC	2495512
Radiation	CuKα (λ = 1.54184 Å)
Empirical formula	$C_{53}H_{62}Au_8B_{20}P_4S_4Cl_2$
M_r *(g mol^{-1})*	2814.07
Temperature/K	100.15
Crystal system	monoclinic
Space group	$P2_1/c$
a/Å	13.3226(17)
b/Å	23.431(3)
c/Å	26.702(4)
α/°	90
β/°	93.581(5)
γ/°	90
Volume/Å^3	8319(2)
Z	4
D_c*/g cm^{-3}*	2.255
F (*000*)	5100.0
Reflections collected	192735
Independent reflections	19124 [R_{int} = 0.2642, R_{sigma} = 0.1298]
GOF on F^2	1.049
Final R indexes [I>=2σ (I)]	R_1 = 0.0650, wR_2 = 0.1688
Final R indexes [all data]	R_1 = 0.0925, wR_2 = 0.1901

$R_1 = \sum(F_o - F_c)/\sum F_o$; $wR_2 = [\sum w(F_o^2 - F_c^2)^2/\sum w(F_o^2)^2]^{1/2}$.

Compound	**$[Au_8S_4(m\text{-}P\text{^}P)_2]$ (b) $Au_{18} + NH_4PF_6$**
CCDC	2454646
Radiation	CuKα (λ = 1.54184 Å)
Empirical formula	$C_{52}H_{60}Au_8B_{20}P_4S_4$
M_r *(g mol^{-1})*	2729.05
Temperature/K	100.15
Crystal system	monoclinic
Space group	$P2_1/c$
a/Å	13.3714(5)
b/Å	23.3899(9)
c/Å	26.9799(9)
α/°	90
β/°	93.7000(10)
γ/°	90
Volume/Å^3	8420.5(5)
Z	4
D_c*/g cm^{-3}*	2.153
F (*000*)	4912.0
Reflections collected	78873
Independent reflections	15103 [R_{int} = 0.0697, R_{sigma} = 0.0490]
GOF on F^2	1.099
Final R indexes [I>=2σ (I)]	R_1 = 0.0386, wR_2 = 0.1016
Final R indexes [all data]	R_1 = 0.0549, wR_2 = 0.1153
$R_1 = \sum(F_o - F_c)/\sum F_o$; $wR_2 = [\sum w(F_o^2 - F_c^2)^2/\sum w(F_o^2)^2]^{1/2}$.	

Compound	**$[Au_8S_4(m\text{-}P\hat{}P)_2]$ (c) $[Au_2(BF_4)_2L_2] + H_2S$**
CCDC	2495510
Radiation	CuKα (λ = 1.54184 Å)
Empirical formula	$C_{52}H_{60}Au_8B_{20}P_4S_4$
M_r *(g mol^{-1})*	2729.05
Temperature/K	100.15
Crystal system	monoclinic
Space group	$P2_1/c$
a/Å	13.314(5)
b/Å	23.337(10)
c/Å	26.678(10)
α/°	90
β/°	93.510(15)
γ/°	90
Volume/Å^3	8274(56)
Z	4
D_c*/g cm^{-3}*	2.191
F (*000*)	4912.0
Reflections collected	36877
Independent reflections	3030 [R_{int} = 0.2694, R_{sigma} = 0.1047]
GOF on F^2	1.045
Final R indexes [I>=2σ (I)]	R_1 = 0.0807, wR_2 = 0.2110
Final R indexes [all data]	R_1 = 0.1091, wR_2 = 0.2428
$R_1 = \sum(F_o - F_c)/\sum F_o$; $wR_2 = [\sum w(F_o^2 - F_c^2)^2/\sum w(F_o^2)^2]^{1/2}$.	

Compound	**$[Au_8S_4(m\text{-}P\hat{}P)_2]$ (d) $Au_2 + S(SiMe_3)_2$**
CCDC	2495511
Radiation	CuKα (λ = 1.54184 Å)
Empirical formula	$C_{52}H_{60}Au_8B_{20}P_4S_4$ C52H60Au8B20P4S4
M_r *(g mol^{-1})*	2729.05
Temperature/K	100.15
Crystal system	monoclinic
Space group	$P2_1/c$
a/Å	13.2101(5)
b/Å	22.4739(8)
c/Å	26.7665(9)
α/°	90
β/°	93.683(2)
γ/°	90
Volume/Å^3	7930.1(5)
Z	4
D_c*/g cm^{-3}*	2.286
F (*000*)	4912.0
Reflections collected	121298
Independent reflections	15103 [R_{int} = 0.0697, R_{sigma} = 0.0490]
GOF on F^2	1.054
Final R indexes [I>=2σ (I)]	R_1 = 0.0760, wR_2 = 0.1978
Final R indexes [all data]	R_1 = 0.1144, wR_2 = 0.2121

$R_1 = \sum(F_o - F_c)/\sum F_o$; $wR_2 = [\sum w(F_o^2 - F_c^2)^2/\sum w(F_o^2)^2]^{1/2}$.

Compound	**[Au_7(*m*-P^P)$_2$(*o*-^{nido}P^P)$_2$]**
CCDC	2504018
Radiation	CuKα (λ = 1.54184 Å)
Empirical formula	$C_{104}H_{120}Au_7B_{38}P_8$
M_r *(g mol^{-1})*	2303.86
Temperature/K	193.15
Crystal system	monoclinic
Space group	*C2/c*
a/Å	20.7101(11)
b/Å	24.5585(12)
c/Å	30.2178(14)
α/°	90
β/°	108.257(3)
γ/°	90
Volume/Å^3	14595.4(13)
Z	4
D_c*/g cm^{-3}*	1.551
F (*000*)	6428.0
Reflections collected	84544
Independent reflections	13433
GOF on F^2	1.033
Final R indexes [I>=2σ (I)]	R_1 = 0.0407, wR_2 = 0.0997
Final R indexes [all data]	R_1 = 0.0521, wR_2 = 0.1051
$R_1 = \sum(F_o - F_c)/\sum F_o$; $wR_2 = [\sum w(F_o^2 - F_c^2)^2/\sum w(F_o^2)^2]^{1/2}$.	

2.4 Selected bond distances (Å) and bond angles (°)

Table S2. Selected bond distances (Å) and bond angles (°)

Au_{18} (*Z'* = 0.5)			
Au(1)−Au(3)	3.058(3)	Au(4)−Au(5)	3.237(3)
Au(1)−Au(2)	3.150(2)	Au(4)−Au(6)	3.039(2)
Au(1)−P(2)	2.271(12)	Au(4)−S(3)	2.355(12)
Au(1)−S(1)	2.339(11)	Au(4)−S(2)	2.341(13)
Au(7)−Au(3)	3.287(3)	Au(2)−P(1)	2.268(14)
Au(7)−Au(3)#1	3.260(3)	Au(2)−S(1)	2.302(12)
Au(7)−Au(4)#1	3.234(3)	Au(8)−Au(9)	3.134(2)
Au(7)−Au(4)	3.363(3)	Au(8)−S(4)	2.319(11)
Au(7)−Au(8)	3.120(3)	Au(8)−P(5)	2.256(14)
Au(7)−Au(9)	3.001(3)	Au(9)−S(4)	2.344(11)
Au(7)−S(4)	2.313(12)	Au(9)−P(6)	2.247(13)
Au(7)−S(2)	2.292(12)	Au(5)−Au(6)	3.177(3)
Au(3)−Au(4)#1	3.323(3)	Au(5)−S(3)	2.316(12)
Au(3)−Au(4)	3.449(2)	Au(5)−P(3)	2.266(13)
Au(3)−Au(2)	3.132(2)	Au(6)−S(3)	2.298(12)
Au(3)−S(2)	2.292(13)	Au(6)−P(4)	2.239(12)
Au(3)−S(1)	2.358(13)		
Au(7)−S(4)−Au(8)	84.7(4)	Au(6)−S(3)−Au(5)	87.0(4)
Au(7)−S(4)−Au(9)	80.3(3)	Au(7)−S(2)−Au(4)	93.1(5)
Au(8)−S(4)−Au(9)	84.5(4)	Au(3)−S(2)−Au(7)	91.6(4)
Au(5)−S(3)−Au(4)	87.7(4)	Au(3)−S(2)−Au(4)	96.2(5)
Au(6)−S(3)−Au(4)	81.5(4)		
Au_{18} (*Z'* = 1.0)			

Au(5)−Au(6)	3.1202(10)	Au(12)−Au(15)	3.2582(10)
Au(5)−Au(4)	3.0943(9)	Au(12)−Au(14)	3.0349(11)
Au(5)−S(3)	2.302(4)	Au(12)−S(6)	2.338(4)
Au(5)−P(4)	2.260(4)	Au(12)−S(7)	2.304(4)
Au(6)−Au(4)	3.0351(10)	Au(7)−S(4)	2.345(4)
Au(6)−S(3)	2.345(4)	Au(7)−S(2)	2.311(4)
Au(6)−P(5)	2.269(4)	Au(16)−Au(15)	3.0244(10)
Au(8)−Au(9)	3.0607(9)	Au(16)−Au(17)	3.1348(11)
Au(8)−Au(7)	2.9939(10)	Au(16)−S(5)	2.330(4)
Au(8)−S(4)	2.327(4)	Au(16)−P(11)	2.264(4)
Au(8)−P(3)	2.251(4)	Au(1)−Au(3)	3.1972(10)
Au(9)−Au(7)	3.0609(10)	Au(1)−S(1)	2.302(4)
Au(9)−S(4)	2.310(4)	Au(1)−P(6)	2.277(5)
Au(9)−P(2)	2.248(4)	Au(11)−Au(15)	3.4730(10)
Au(4)−Au(2)	3.4200(9)	Au(11)−Au(15)#2	3.2408(10)
Au(4)−Au(2)#1	3.2586(9)	Au(11)−Au(18)	3.0494(10)
Au(4)−Au(7)	3.2990(10)	Au(11)−Au(10)	3.1572(10)
Au(4)−Au(7)1	3.1965(10)	Au(11)−S(8)	2.356(4)
Au(4)−S(3)	2.338(4)	Au(11)−S(7)	2.305(5)
Au(4)−S(2)	2.304(4)	Au(3)−S(1)	2.310(4)
Au(2)−Au(7)#1	3.1701(9)	Au(3)−P(1)	2.246(4)
Au(2)−Au(7)	3.3866(10)	Au(15)−Au(17)	3.1250(10)
Au(2)−Au(1)	3.2182(10)	Au(15)−S(7)	2.309(4)
Au(2)−Au(3)	3.0548(9)	Au(15)−S(5)	2.348(4)
Au(2)−S(1)	2.339(4)	Au(18)−Au(10)	3.2652(10)
Au(2)−S(2)	2.302(4)	Au(18)−S(8)	2.314(4)
Au(13)−Au(12)	3.0740(10)	Au(18)−P(10)	2.259(4)
Au(13)−Au(14)	3.0852(10)	Au(14)−S(6)	2.314(4)

Au(13)−P(9)	2.252(4)	Au(14)−P(8)	2.254(5)
Au(13)−S(6)	2.313(4)	Au(10)−S(8)	2.310(4)
Au(5)−S(3)−Au(6)	84.36(12)	Au(1)−S(1)−Au(2)	87.80(13)
Au(5)−S(3)−Au(4)	83.64(13)	Au(1)−S(1)−Au(3)	87.78(13)
Au(4)−S(3)−Au(6)	80.80(13)	Au(3)−S(1)−Au(2)	82.14(13)
Au(8)−S(4)−Au(7)	79.71(13)	Au(18)−S(8)−Au(11)	81.53(15)
Au(9)−S(4)−Au(8)	82.61(13)	Au(10)−S(8)−Au(11)	85.16(14)
Au(9)−S(4)−Au(7)	82.22(13)	Au(10)−S(8)−Au(18)	89.85(15)

Au_8 (Au_{18} + NH_4BF_4)

Au(3)−Au(4)	2.9518(8)	Au(5)−P(00P)	2.261(4)
Au(3)−Au(2)	3.1402(8)	Au(2)−Au(1)	3.0270(8)
Au(3)−S(00J)	2.323(3)	Au(2)−Au(8)	3.3146(9)
Au(3)−P(00L)	2.251(4)	Au(2)−S(00J)	2.304(4)
Au(4)−Au(5)	2.9339(8)	Au(2)−S(00T)	2.312(4)
Au(4)−Au(2)	3.2373(9)	Au(7)−Au(6)	2.9618(9)
Au(4)−Au(6)	3.2876(8)	Au(7)−Au(8)	3.1027(9)
Au(4)−S(00J)	2.328(4)	Au(7)−S(00V)	2.320(4)
Au(4)−S(00Q)	2.327(4)	Au(7)−P(00W)	2.250(4)
Au(5)−Au(6)	3.1984(9)	Au(1)−Au(8)	3.0012(10)
Au(5)−S(00Q)	2.315(4)		
Au(3)−S(00J)−Au(4)	78.78(11)	Au(2)−S(00T)−Au(1)	81.44(14)
Au(2)−S(00J)−Au(3)	85.48(12)	Au(2)−S(00T)−Au(8)	91.54(16)
Au(2)−S(00J)−Au(4)	88.67(13)	Au(8)−S(00T)−Au(1)	80.56(13)
Au(5)−S(00Q)−Au(4)	78.39(11)	Au(7)−S(00V)−Au(6)	79.12(12)
Au(5)−S(00Q)−Au(6)	87.18(14)	Au(8)−S(00V)−Au(7)	84.19(14)

Au_8 (Au_{18} + NH_4PF_6)

Au(2)−Au(3)	2.9366(5)	Au(7)−Au(6)	3.1062(6)
Au(2)−Au(4)	3.1888(5)	Au(7)−P(2)	2.259(2)
Au(2)−Au(1)	2.9350(5)	Au(7)−S(4)	2.329(2)
Au(2)−Au(8)	3.3364(6)	Au(5)−Au(6)	3.0070(6)
Au(2)−S(2)	2.328(2)	Au(5)−P(4)	2.253(3)
Au(2)−S(1)	2.328(3)	Au(5)−S(3)	2.325(2)
Au(3)−Au(4)	3.1151(5)	Au(1)−Au(8)	3.2896(6)
Au(3)−S(2)	2.324(2)	Au(1)−S(1)	2.318(2)
Au(3)−P(1)	2.257(2)	Au(1)−P(3)	2.251(2)
Au(4)−Au(5)	2.9938(5)	Au(8)−Au(6)	3.2039(6)
Au(4)−Au(6)	3.3645(6)	Au(8)−S(1)	2.313(2)
Au(4)−S(2)	2.312(2)	Au(8)−S(4)	2.332(3)
Au(4)−S(3)	2.318(2)		

Au(1)−S(1)−Au(2)	78.35(8)	Au(4)−S(3)−Au(5)	80.31(8)
Au(8)−S(1)−Au(2)	91.92(9)	Au(6)−S(3)−Au(4)	93.26(9)
Au(8)−S(1)−Au(1)	90.53(9)	Au(6)−S(3)−Au(5)	80.89(8)
Au(7)−S(4)−Au(8)	78.81(7)	Au(3)−S(2)−Au(2)	78.29(8)
Au(6)−S(4)−Au(7)	84.26(8)	Au(4)−S(2)−Au(2)	86.81(8)
Au(6)−S(4)−Au(8)	87.49(9)	Au(4)−S(2)−Au(3)	84.44(8)

Au_8 (Au_2(m-P^P)$_2$[BF_4]$_2$+ H_2S)

Au(4)−Au(3)	2.954(5)	Au(5)−S(00L)	2.29(2)
Au(4)−Au(5)	3.127(5)	Au(5)−S(00T)	2.32(2)
Au(4)−S(00L)	2.33(2)	Au(1)−Au(2)	2.962(5)
Au(4)−P(00S)	2.27(3)	Au(1)−Au(7)	3.084(5)

Au(3)−Au(8)	2.935(5)	Au(1)−S(00H)	2.35(2)
Au(3)−Au(5)	3.233(5)	Au(1)−P(00N)	2.27(3)
Au(3)−Au(2)	3.292(5)	Au(2)−Au(7)	3.228(6)
Au(3)−S(00I)	2.32(2)	Au(2)−S(00H)	2.35(2)
Au(3)−S(00L)	2.34(2)	Au(2)−S(00I)	2.34(2)
Au(8)−Au(2)	3.182(5)	Au(6)−Au(7)	3.003(5)
Au(8)−S(00I)	2.32(2)	Au(6)−S(00T)	2.31(2)
Au(8)−P(00M)	2.25(3)	Au(6)−P(00U)	2.25(3)
Au(5)−Au(6)	3.034(5)	Au(7)−S(00H)	2.30(2)
Au(5)−Au(7)	3.320(5)	Au(7)−S(00T)	2.33(2)

Au(2)−S(00H)−Au(1)	78.1(7)	Au(4)−S(00L)−Au(3)	78.6(7)
Au(7)−S(00H)−Au(1)	82.9(7)	Au(5)−S(00L)−Au(4)	85.4(8)
Au(7)−S(00H)−Au(2)	87.9(8)	Au(5)−S(00L)−Au(3)	88.7(8)
Au(3)−S(00I)−Au(8)	78.5(7)	Au(5)−S(00T)−Au(7)	91.0(8)
Au(3)−S(00I)−Au(2)	89.9(7)	Au(6)−S(00T)−Au(5)	81.7(8)
Au(8)−S(00I)−Au(2)	86.1(8)	Au(6)−S(00T)−Au(7)	80.6(7)

Au_8 (Au_2Cl_2(*m*-P^P) + SSi_2Me_6)

Au(5)−Au(4)	2.9669(10)	Au(4)−S(3)	2.329(4)
Au(5)−Au(6)	2.9844(11)	Au(4)−S(4)	2.323(4)
Au(5)−S(3)	2.312(4)	Au(7)−Au(1)	3.0920(9)
Au(5)−P(2)	2.247(4)	Au(7)−Au(6)	3.2790(10)
Au(2)−Au(3)	2.9210(9)	Au(7)−Au(8)	3.1005(9)
Au(2)−Au(4)	3.2955(9)	Au(7)−S(1)	2.316(4)
Au(2)−Au(7)	3.2558(10)	Au(7)−S(2)	2.313(5)
Au(2)−Au(1)	2.9950(9)	Au(1)−S(1)	2.322(4)
Au(2)−S(1)	2.319(5)	Au(1)−P(1)	2.256(4)

Au(2)−S(4)	2.327(5)	Au(6)−Au(8)	2.9356(11)
Au(3)−Au(4)	3.0680(9)	Au(6)−S(3)	2.327(5)
Au(3)−S(4)	2.331(4)	Au(6)−S(2)	2.328(5)
Au(3)−P(3)	2.258(4)	Au(8)−S(2)	2.335(4)
Au(4)−Au(6)	3.2479(11)	Au(8)−P(4)	2.257(4)
Au(5)−S(3)−Au(4)	79.47(12)	Au(7)−S(2)−Au(6)	89.91(18)
Au(5)−S(3)−Au(6)	80.07(13)	Au(7)−S(2)−Au(8)	83.69(16)
Au(6)−S(3)−Au(4)	88.46(14)	Au(6)−S(2)−Au(8)	78.03(15)
Au(2)−S(1)−Au(1)	80.38(14)	Au(2)−S(4)−Au(3)	77.67(14)
Au(7)−S(1)−Au(2)	89.26(14)	Au(4)−S(4)−Au(2)	90.26(16)
Au(7)−S(1)−Au(1)	83.64(13)	Au(4)−S(4)−Au(3)	82.49(13)
Au_7			
Au(1)−Au(2)	2.6377(4)	Au(2)−Au(3)	2.7173(3)
Au(1)−Au(4)#1	3.2139(5)	Au(2)−P(55)	2.3581(16)
Au(1)−Au(3)	2.7858(3)	Au(2)−P(37)	2.4019(18)
Au(1)−P(12)	2.3094(18)	Au(4)−Au(3)	2.6834(4)
Au(2)−Au(4)#1	2.6177(4)	Au(4)−Au(3)	2.2881(19)

Symmetry codes for **Au_{18}** (***Z'* = 0.5**) #1 1 − *x*, 1 − *y*, 1 − *z*; **Au_{18}** (***Z'* = 1.0**) #1 1 − *x*, 1 − *y*, 1 − *z*; #2 1 − *x*, 2 − *y*, 2 – *z*; **Au_7** (***Z'* = 1.0**) #1 1 − *x*, + *y*, 1/2 – *z*.

2.5 Crystal structure figures

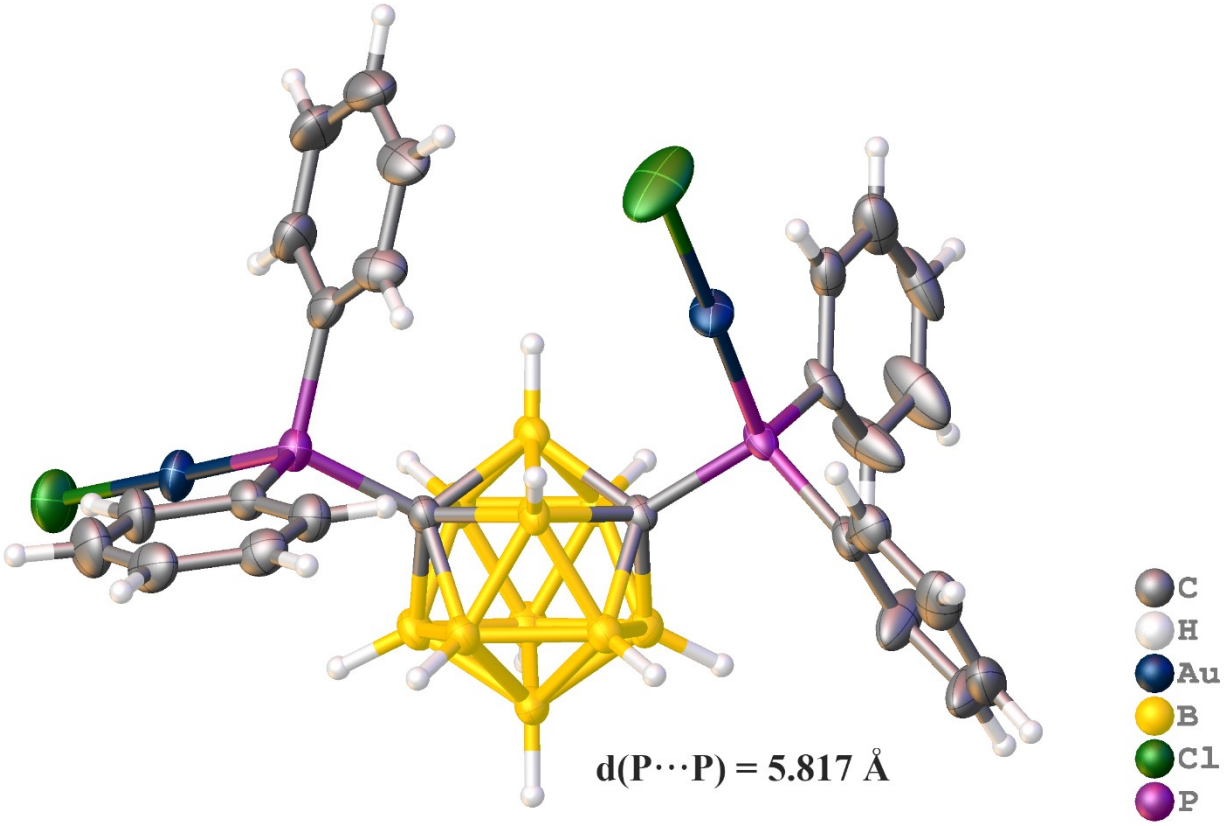

Figure S4. The ellipses & sticks models of **[Au_2Cl_2(*m*-P^P)]**. Thermal ellipsoids are shown at the 50% probability level. The distance between two P atoms is 5.817 Å.

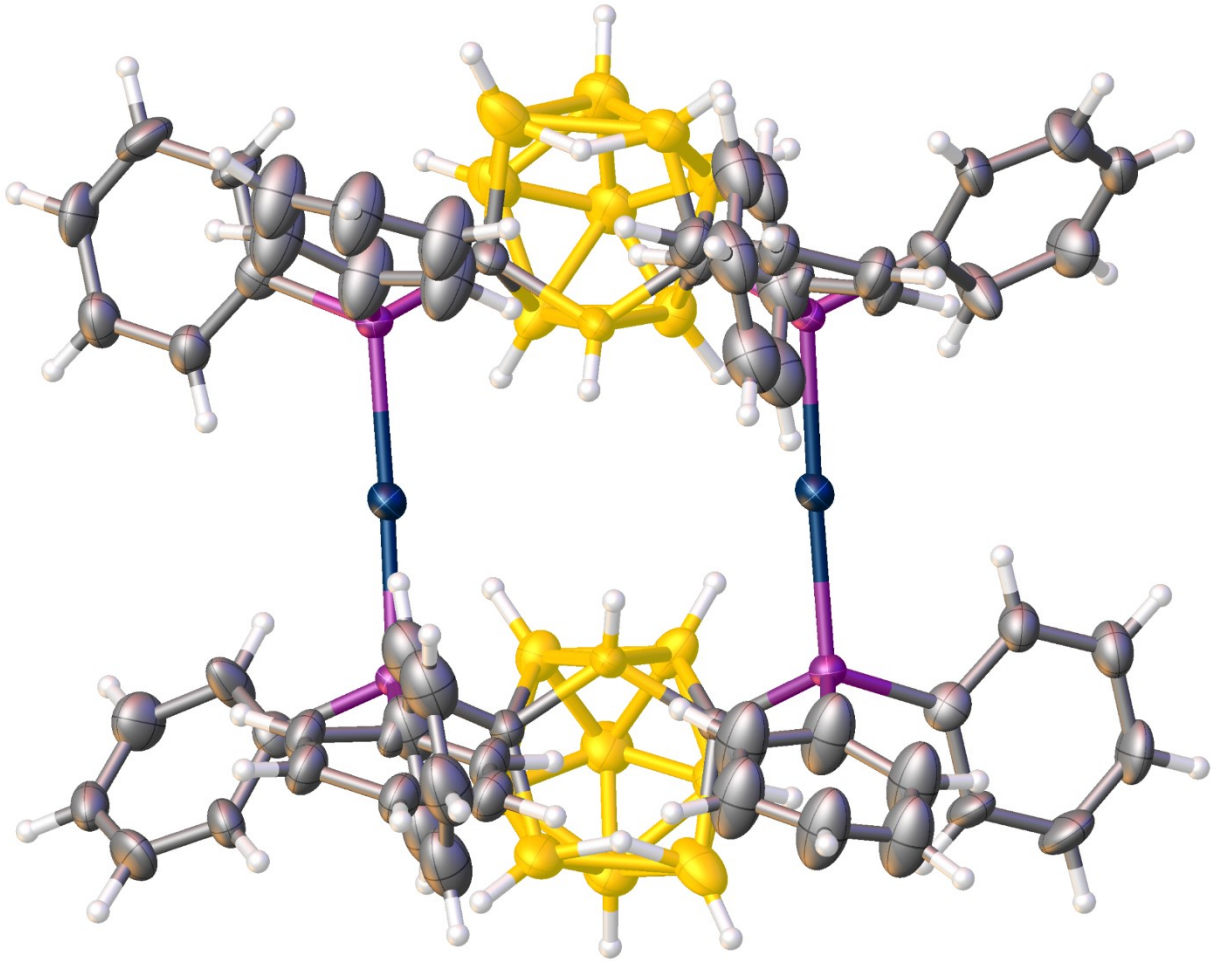

Figure S5. The ellipses & sticks models of **[Au_2(*m*-^{nido}P^P)$_2$]**. Thermal ellipsoids are shown at the 50% probability level. The distance between two P atoms is 5.569 Å.

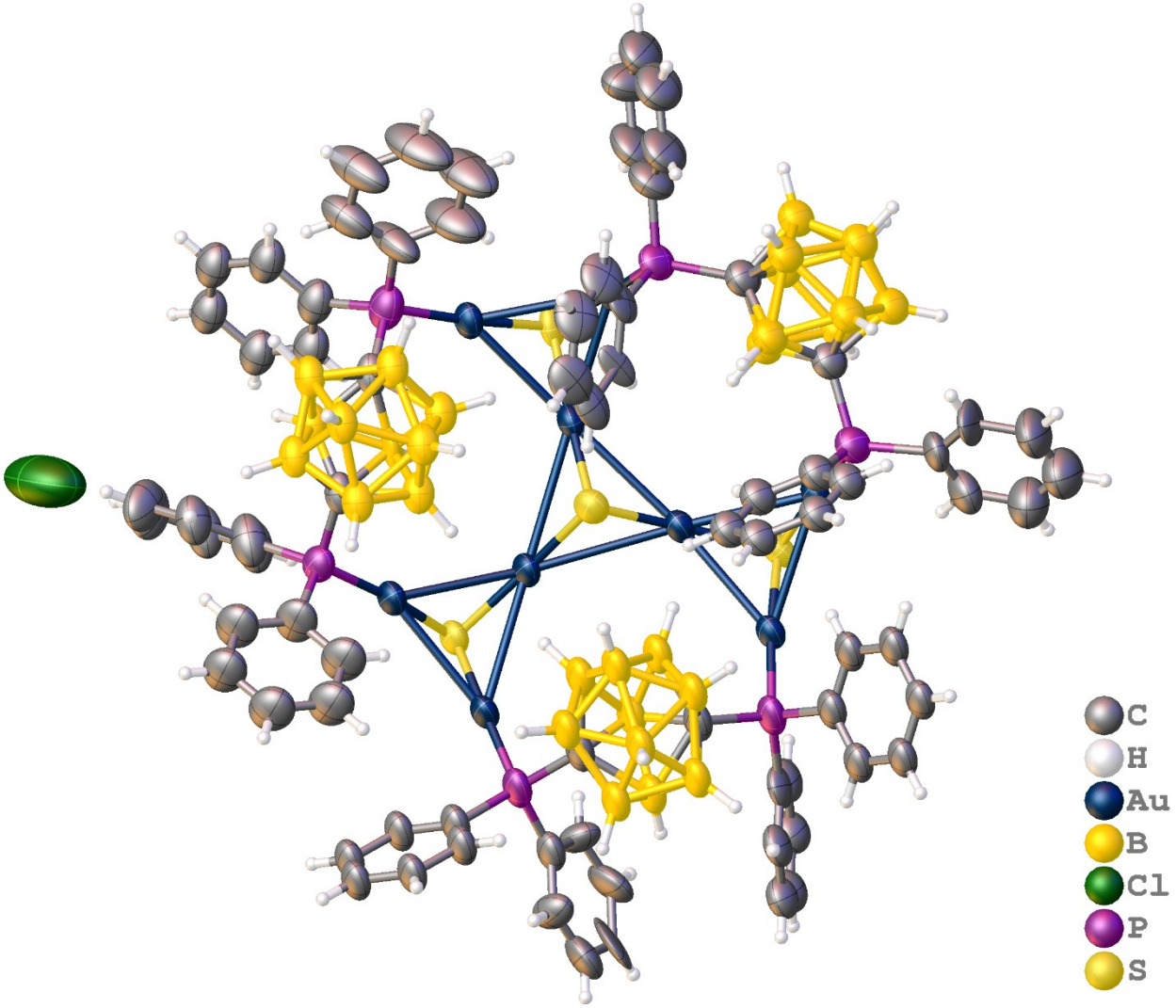

Figure S6. Minimum asymmetric unit of **[$Au_{18}S_8$(*m*-P^P)$_6$][Cl_2] (*Z'* = 0.5)** exhibits as ellipses & sticks models. Thermal ellipsoids are shown at the 50% probability level.

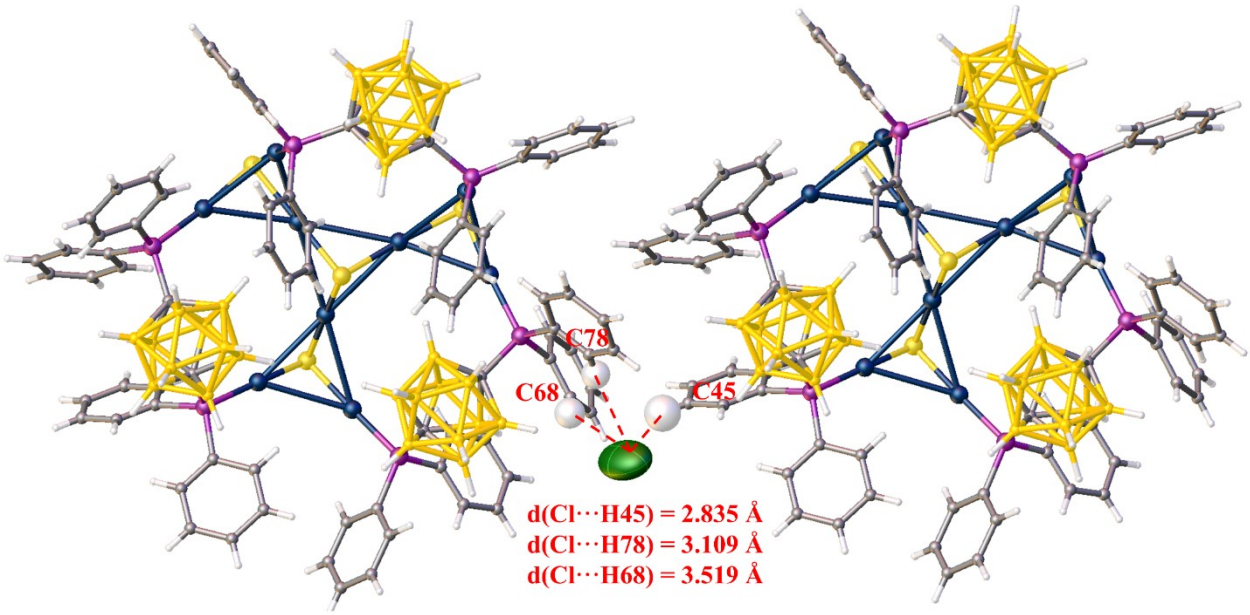

Figure S7. The distances between Cl^- anion and surrounding H atoms in **[$Au_{18}S_8$(*m*-P^P)$_6$][Cl_2] (*Z'* = 0.5)**.

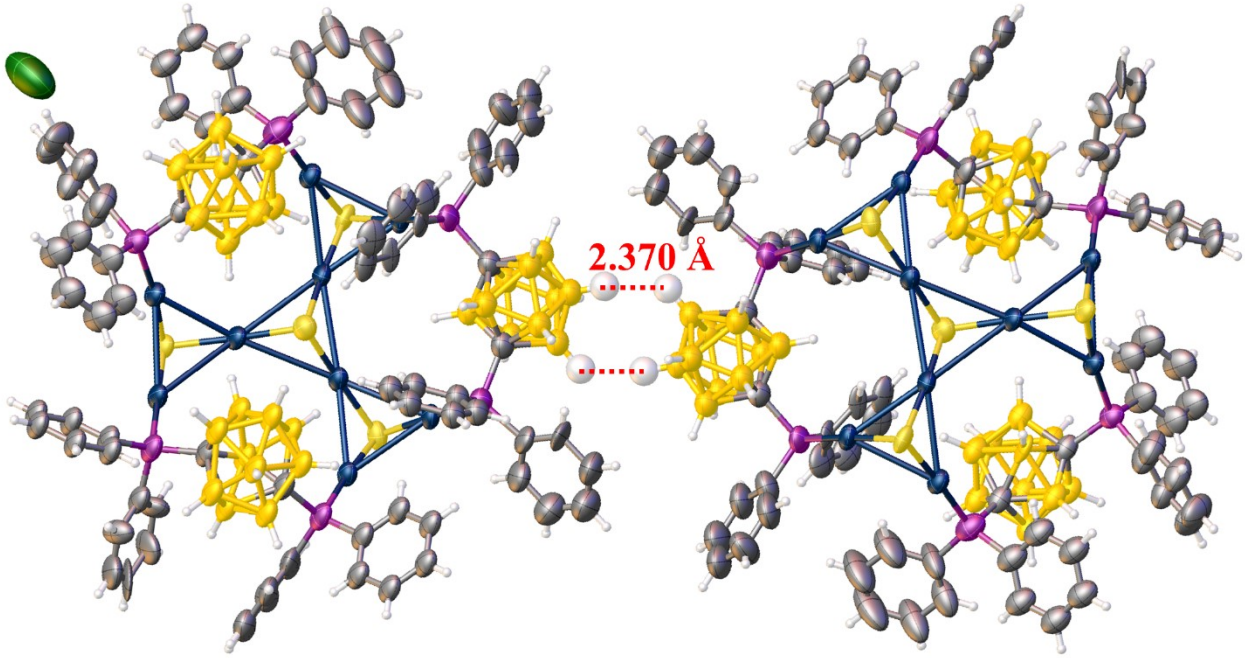

Figure S8. The potential dihydrogen bonds in **[$Au_{18}S_8$(*m*-P^P)$_6$][Cl_2] (*Z'* = 0.5)**.

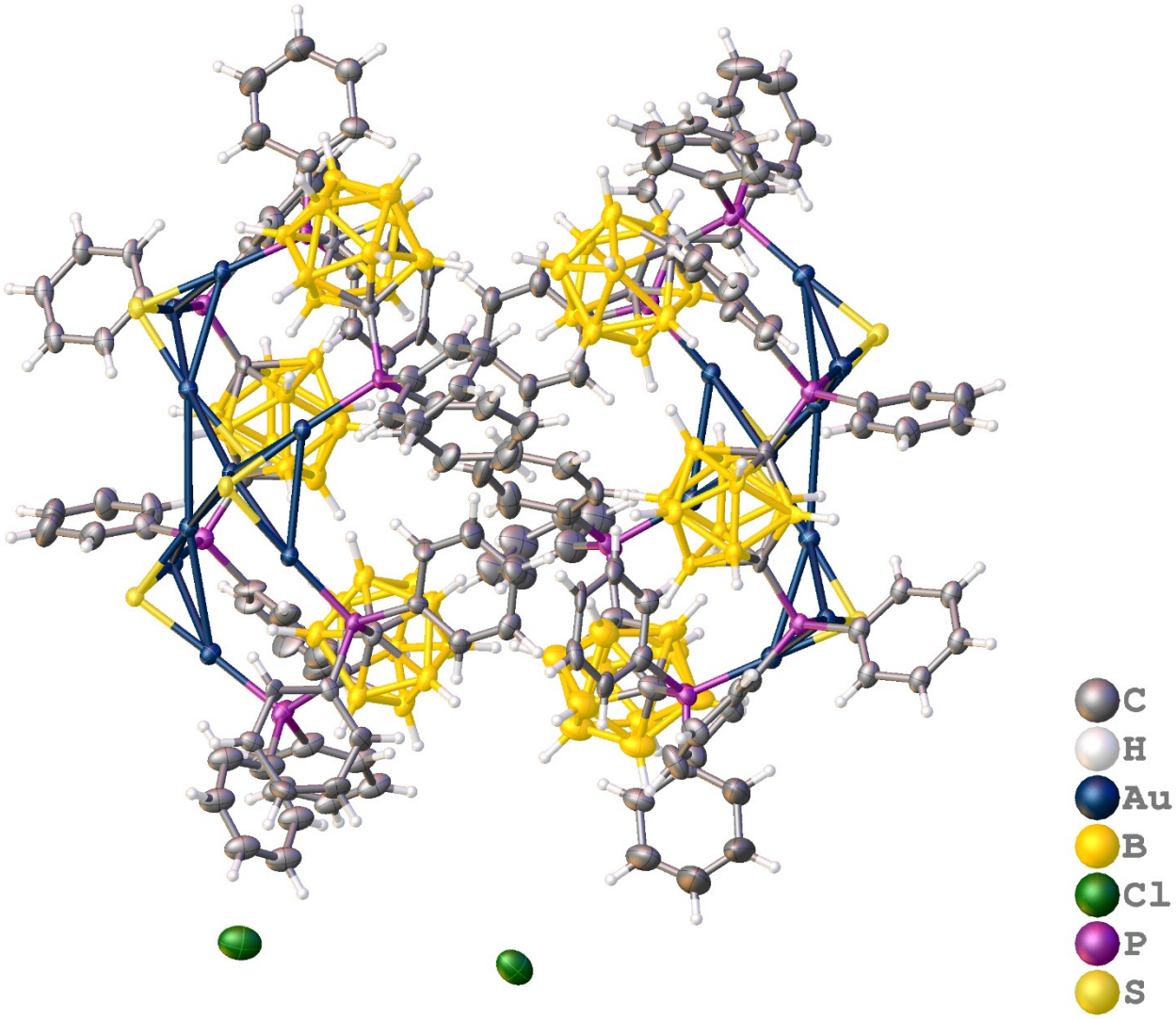

Figure S9. Minimum asymmetric unit of **[$Au_{18}S_8$(*m*-P^P)$_6$][Cl_2] (*Z'* = 1.0)** exhibits as ellipses & sticks models. Thermal ellipsoids are shown at the 50% probability level.

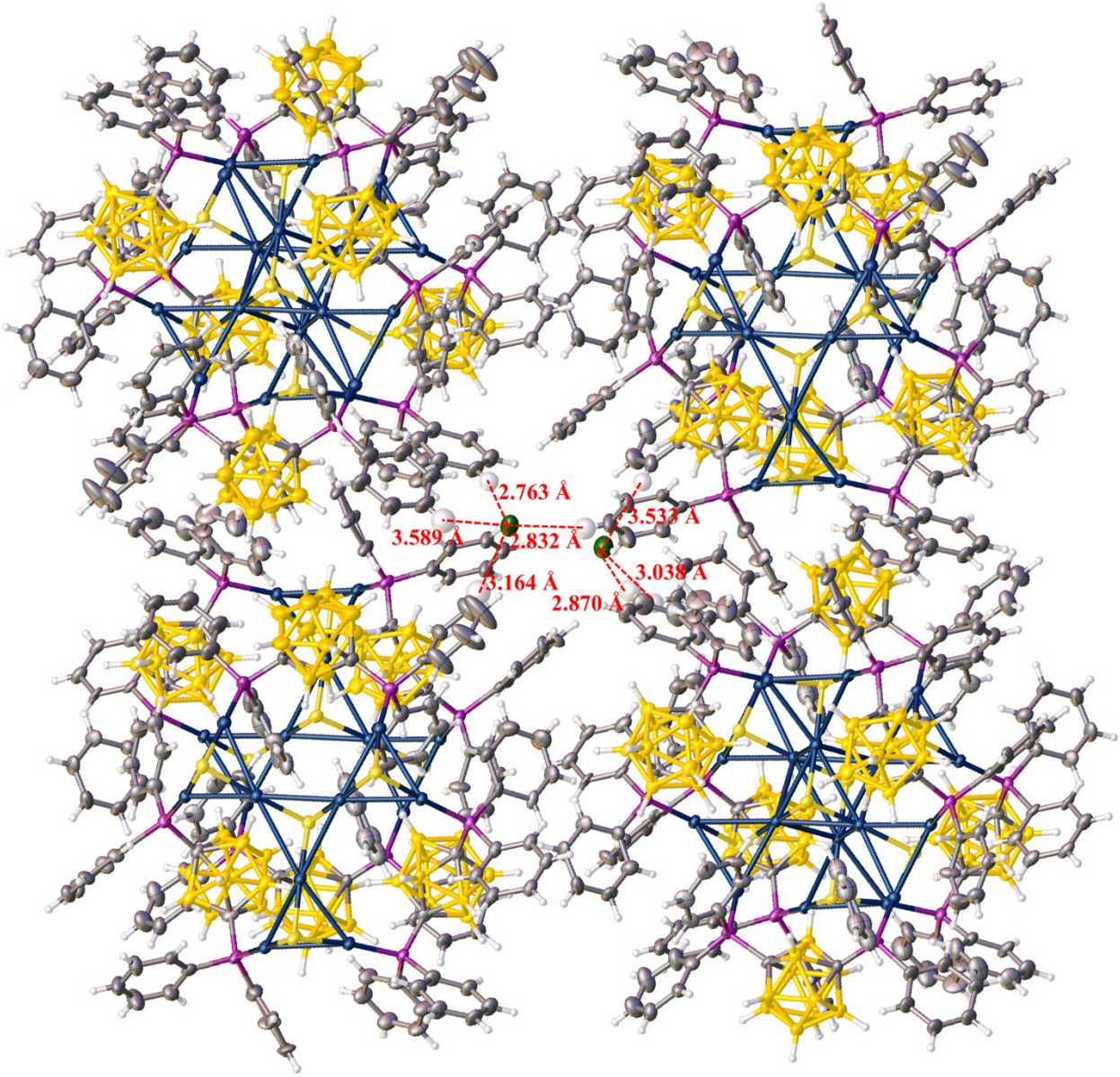

Figure S10. The distances between Cl^- anion and surrounding H atoms in **$[Au_{18}S_8(m\text{-P\^{}P})_6][Cl_2]$ (Z' = 1.0)**.

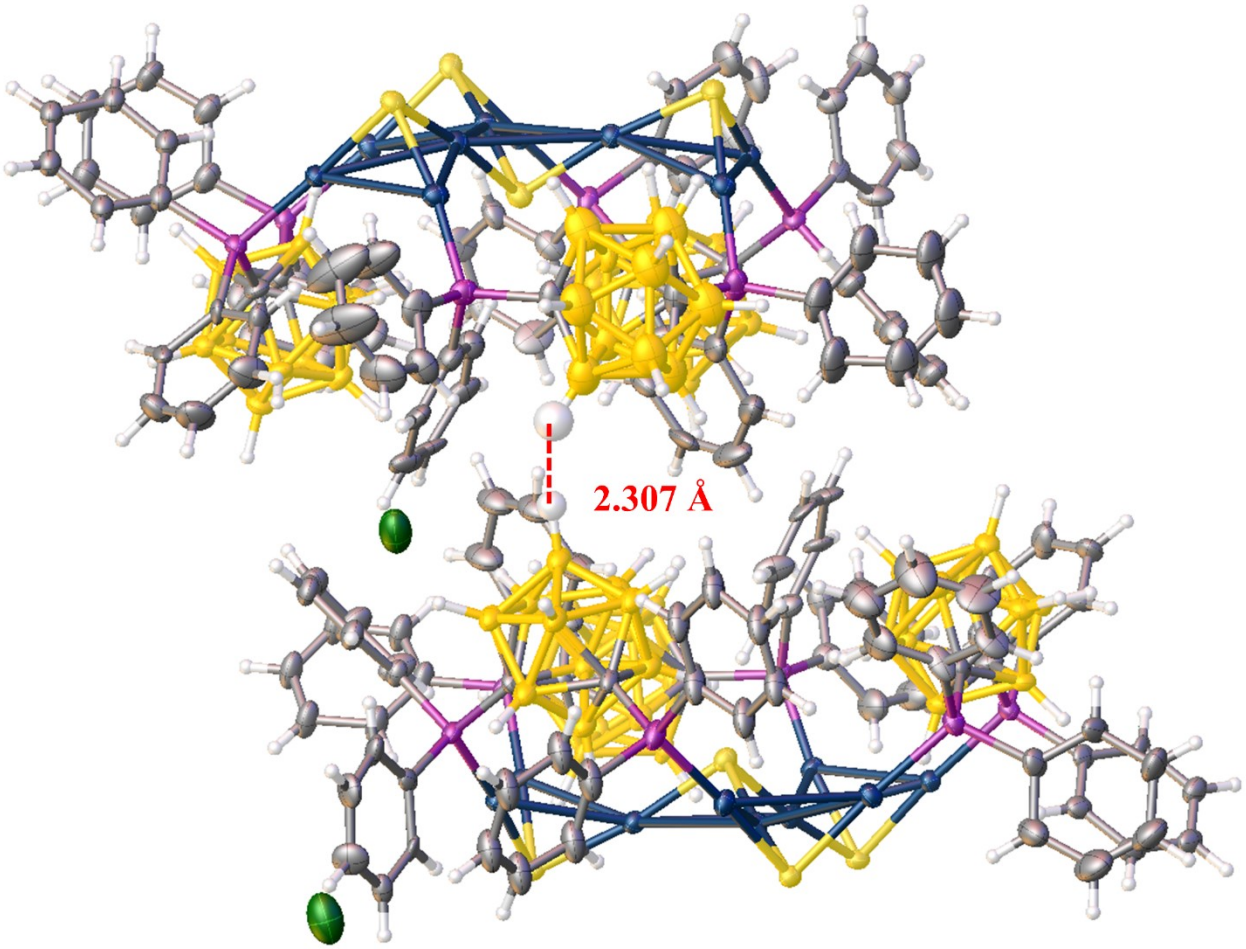

Figure S11. The potential dihydrogen bonds in **[$Au_{18}S_8$(*m*-P^P)$_6$][Cl_2] (*Z'* = 1.0)**.

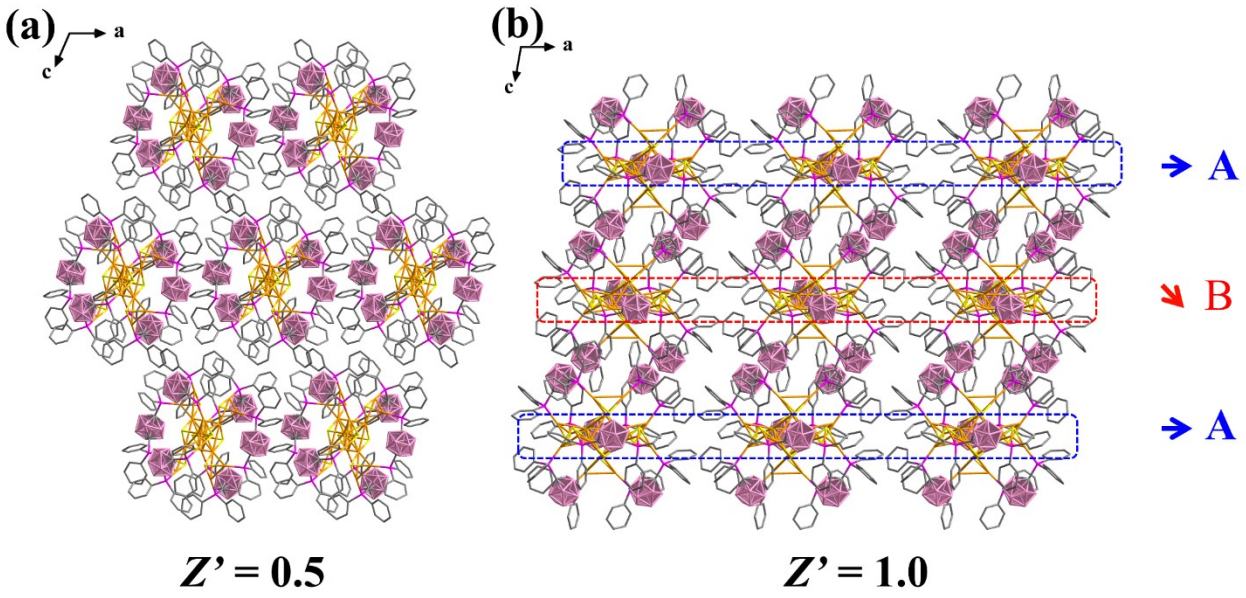

Figure S12. The packing modes of **[$Au_{18}S_8$(*m*-P^P)$_6$][Cl]$_2$** in (a) *Z'* = 0.5 and (b) *Z'* = 1.0.

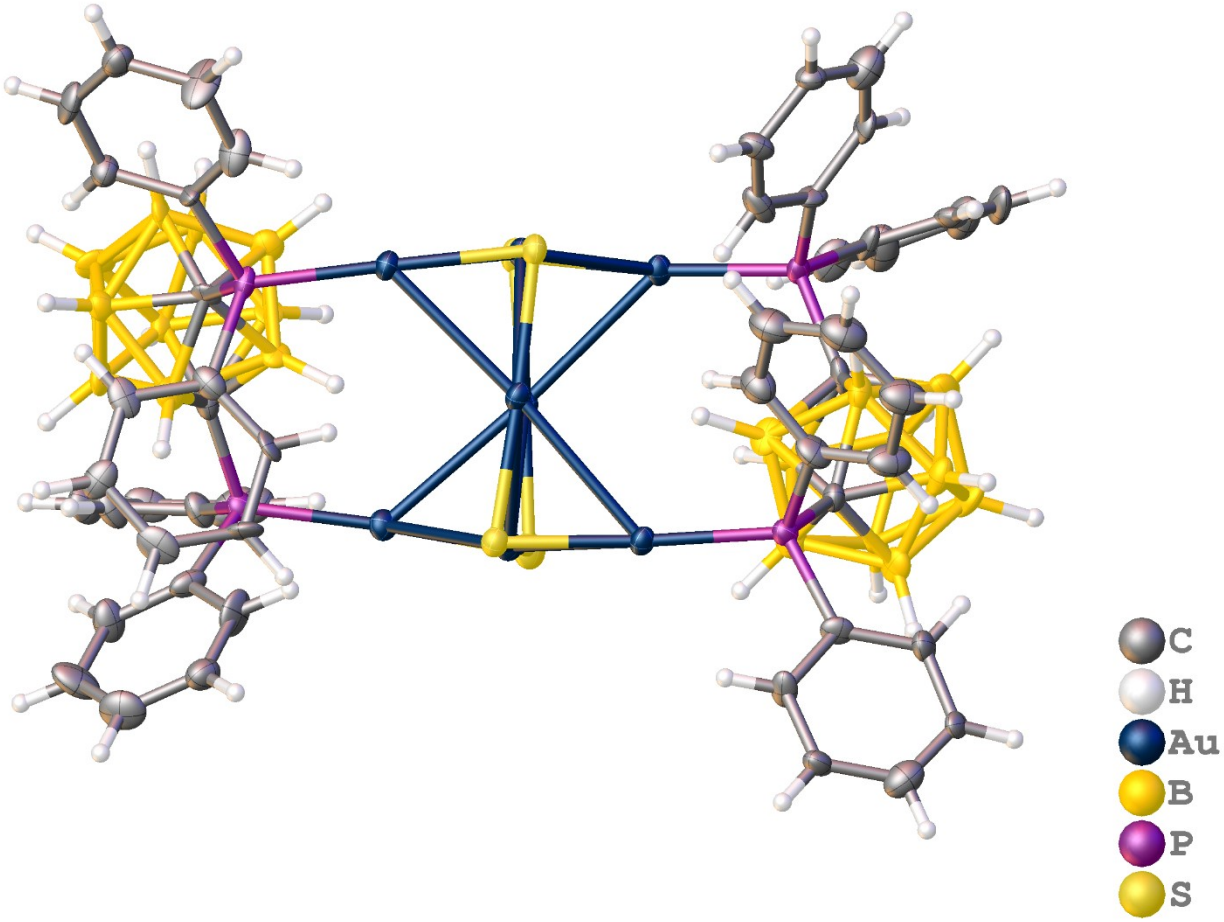

Figure S13. Minimum asymmetric unit of **[Au_8S_4(*m*-P^P)$_2$]** exhibits as ellipses & sticks models. Thermal ellipsoids are shown at the 50% probability level.

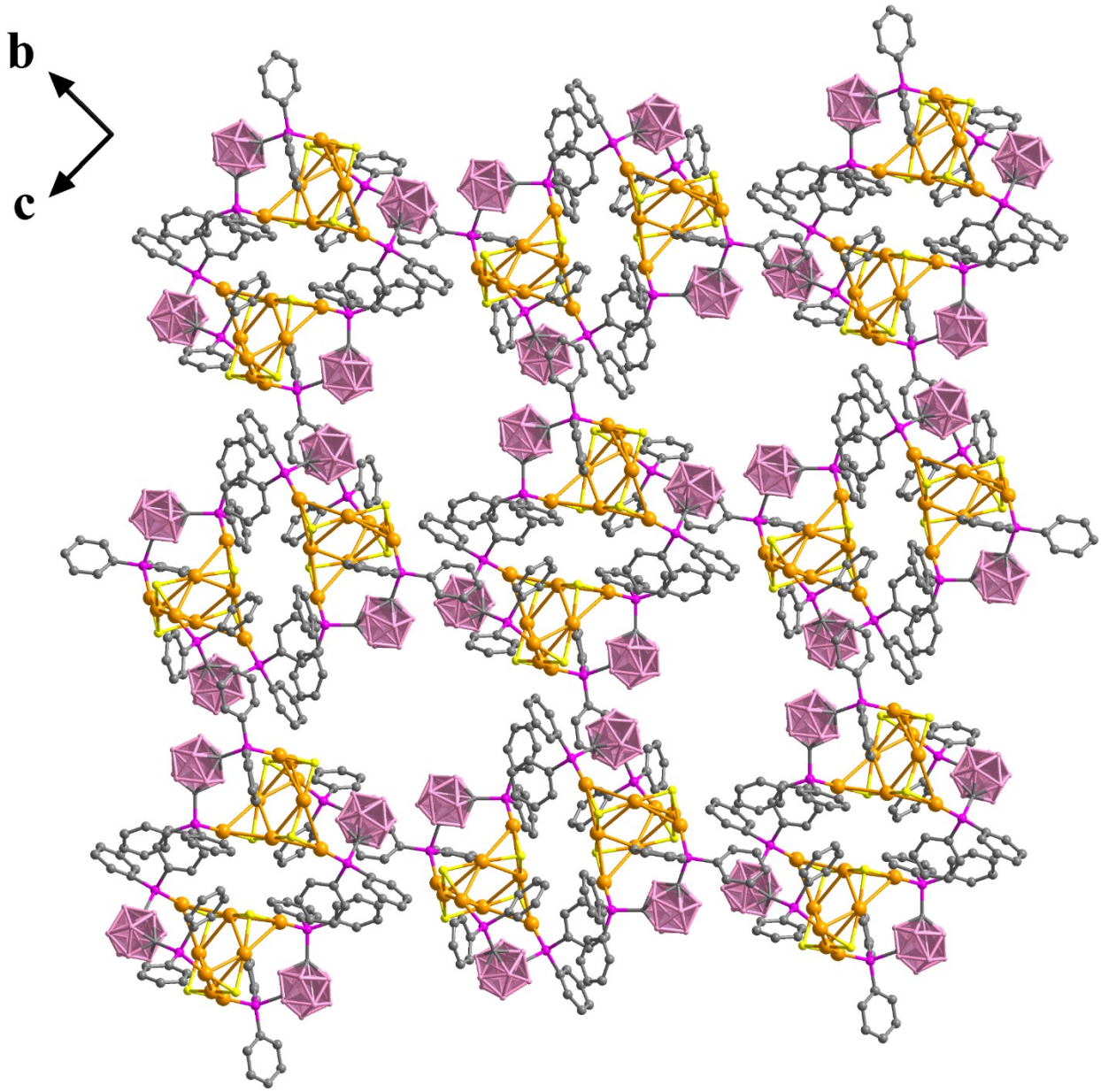

Figure S14. Packing modes of **[Au_8S_4(*m*-P^P)$_2$]** in *bc* plane.

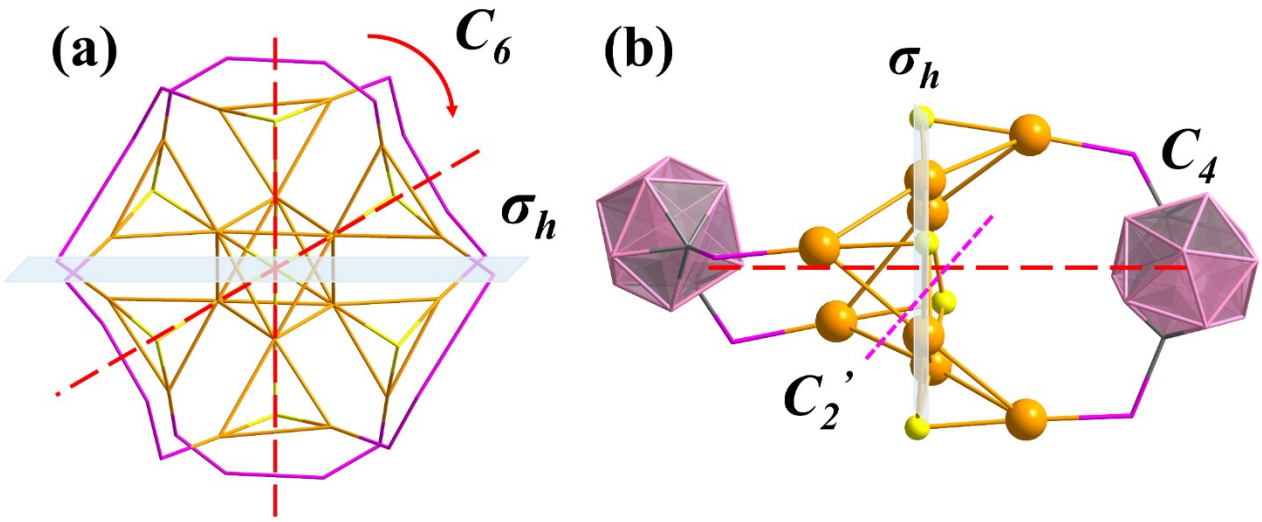

Figure S15. Symmetry operation of (a) **[$Au_{18}S_8$(*m*-P^P)$_6$]$^{2+}$** and (b) **[Au_8S_4(*m*-P^P)$_2$]** at low concentration.

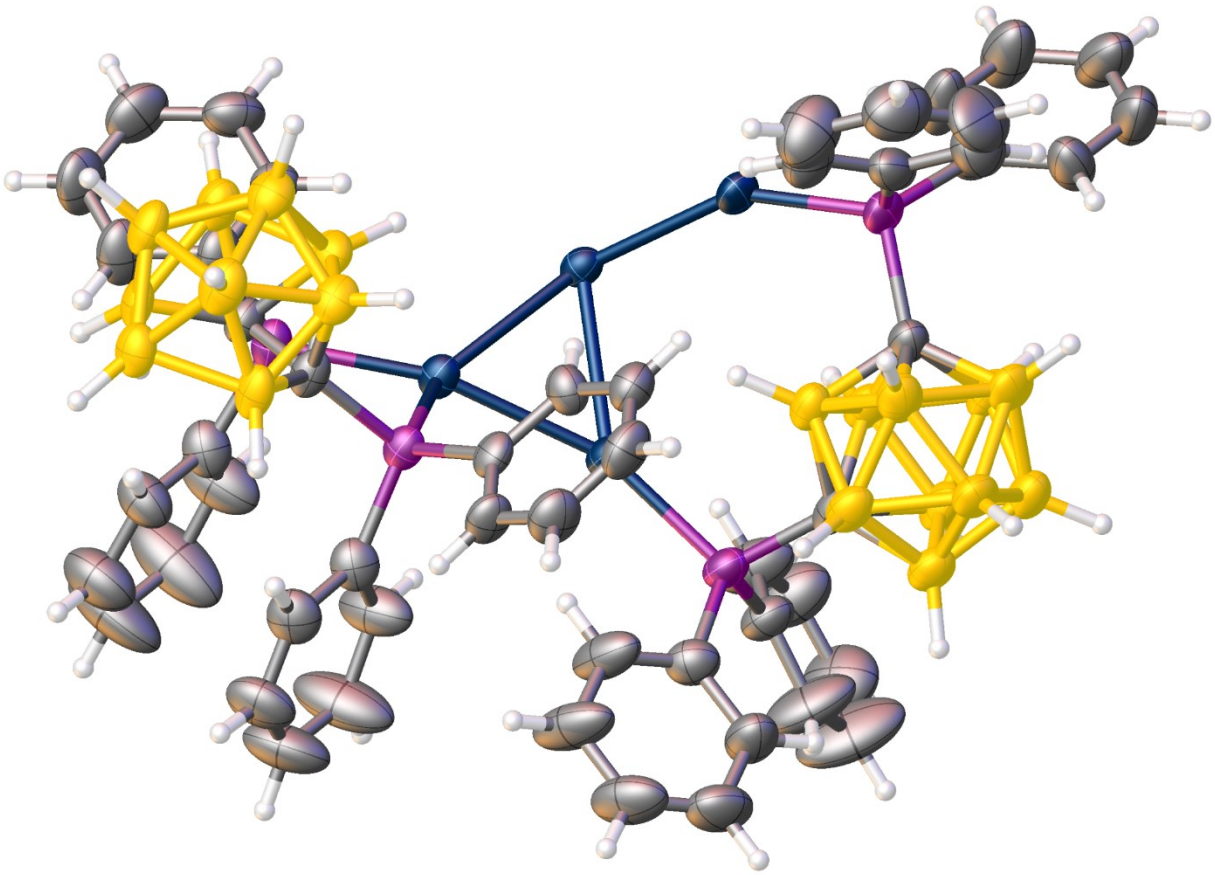

Figure S16. Minimum asymmetric unit of **[Au_7(*m*-P^P)$_2$(*o*-^{nido}P^P)$_2$]** exhibits as ellipses & sticks models. Thermal ellipsoids are shown at the 50% probability level.

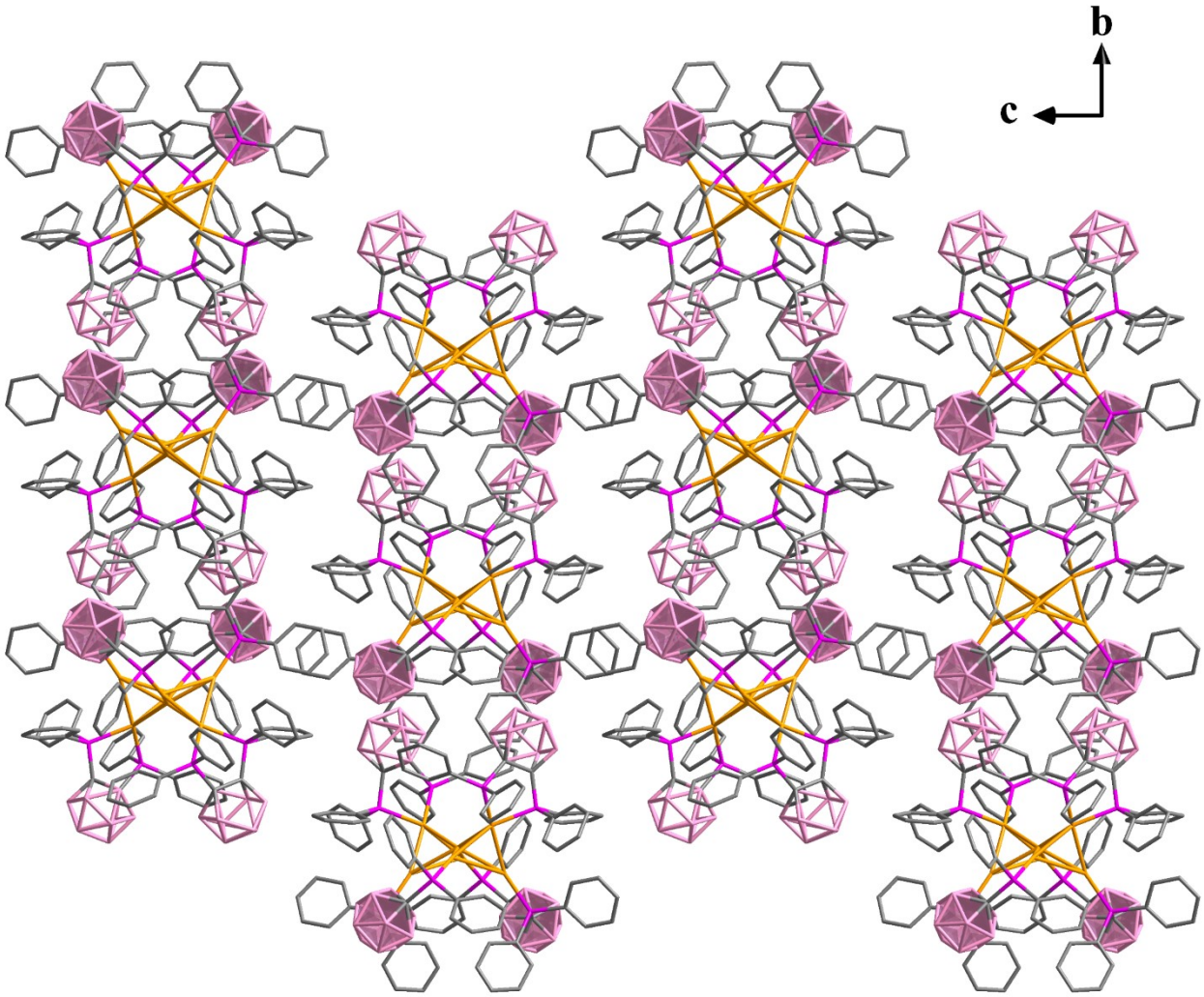

Figure S17. Packing modes of **[Au_4(*m*-P^P)(*o*-^{nido}P^P)$_2$]** in *bc* plane.

3. NMR data

Table S3. ^{31}P NMR Chemical Shifts in $CDCl_3$.

Compounds	*m*-P^P	*o*-P^P	Au_2Cl_2(*m*-P^P)	$[Au_2(m\text{-P^P})_2][BF_4]_2$	Au_7
ppm	20.19	7.20	57.11	57.50(57.02)[a]	95.80, 60.61, 59.99

[a] with minor byproduct $[Au_2(m^{nido}\text{-P^P})_2]$

Table S4. Concentration-dependent ^{31}P NMR Chemical Shifts in $CDCl_3$.

Compounds	Au_{18}			Au_8		
Concentration (mg/μL)	0.02	0.05	0.08	0.02	0.06	0.08
ppm	50.23	50.21, 50.87, 51.67	50.22, 50.78, 51.70	48.00	48.00, 48.14	47.99, 48.14

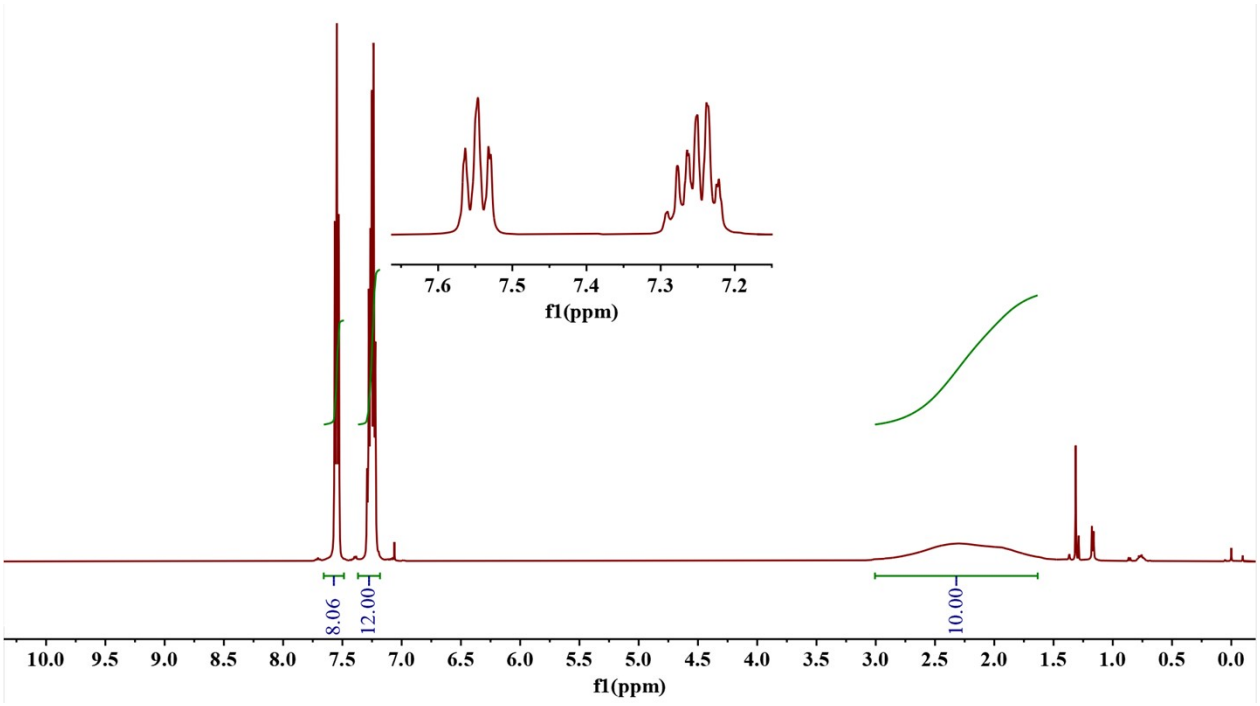

Figure S18. ^{1}H NMR (500 MHz, $CDCl_3$, ppm, 298 K) of ***m*-P^P**.

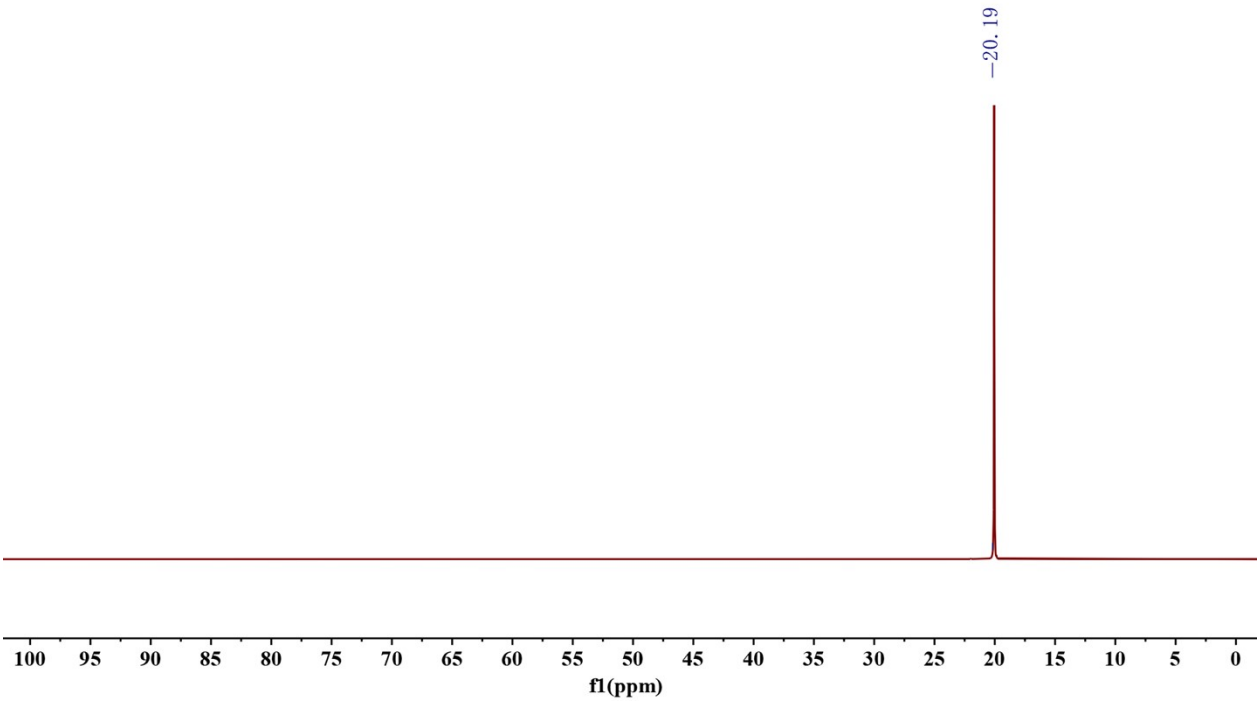

Figure S19. ^{31}P {^{1}H} NMR (202 MHz, $CDCl_3$, ppm, 298 K) of ***m*-P^P**.

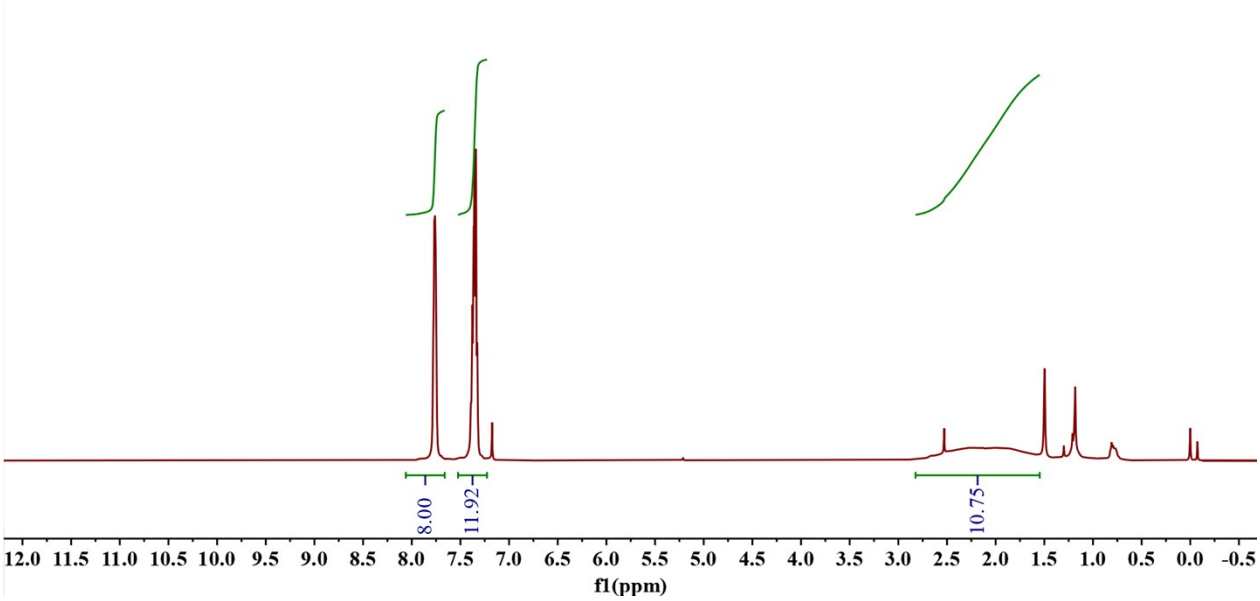

Figure S20. ^{1}H NMR (500 MHz, $CDCl_3$, ppm, 298 K) of ***o*-P^P**.

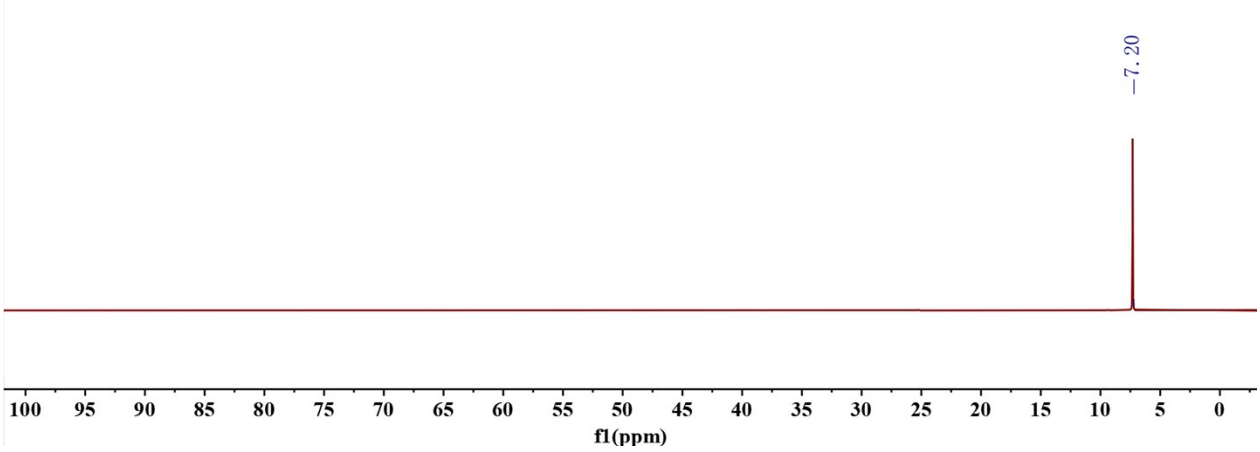

Figure S21. ^{31}P {^{1}H} NMR (202 MHz, $CDCl_3$, ppm, 298 K) of ***o*-P^P**.

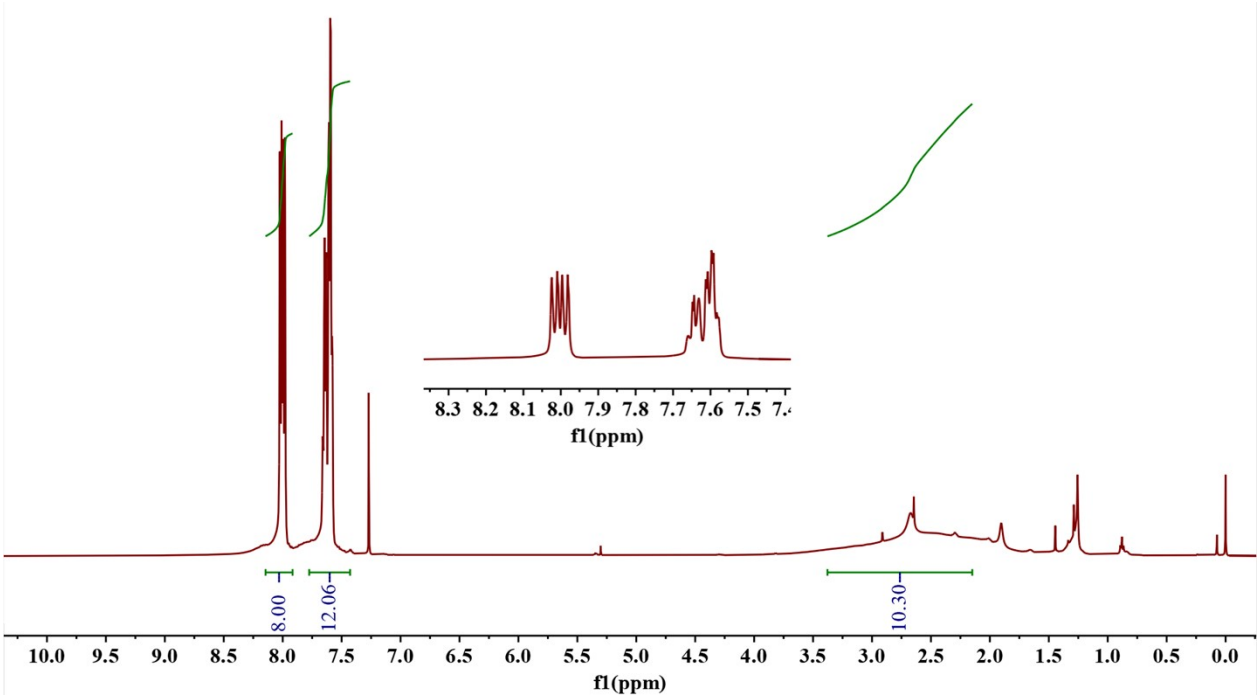

Figure S22. ^{1}H NMR (500 MHz, $CDCl_3$, ppm, 298 K) of **[Au_2Cl_2(*m*-P^P)]**.

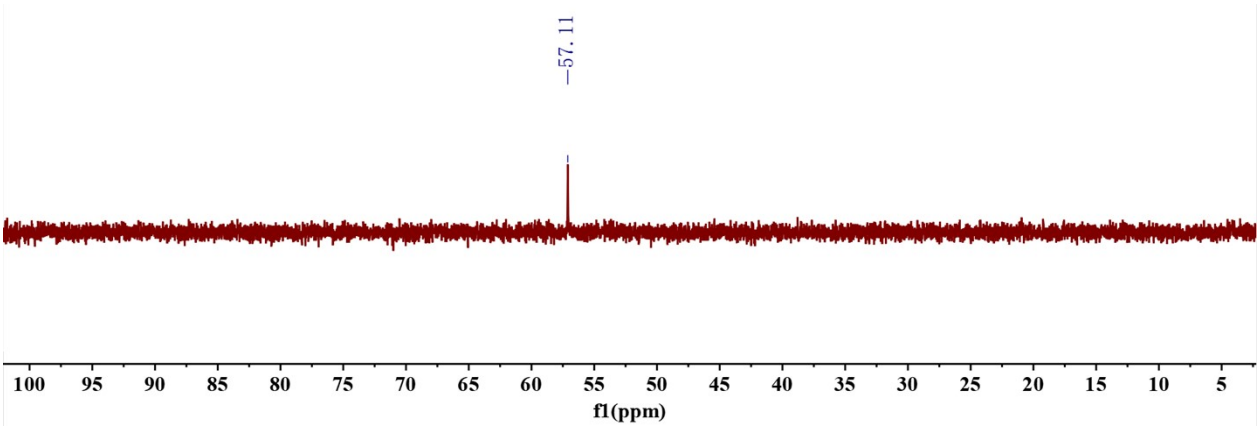

Figure S23. ^{31}P NMR (202 MHz, CD_3CN, ppm, 298 K) of **[Au_2Cl_2(*m*-P^P)]**.

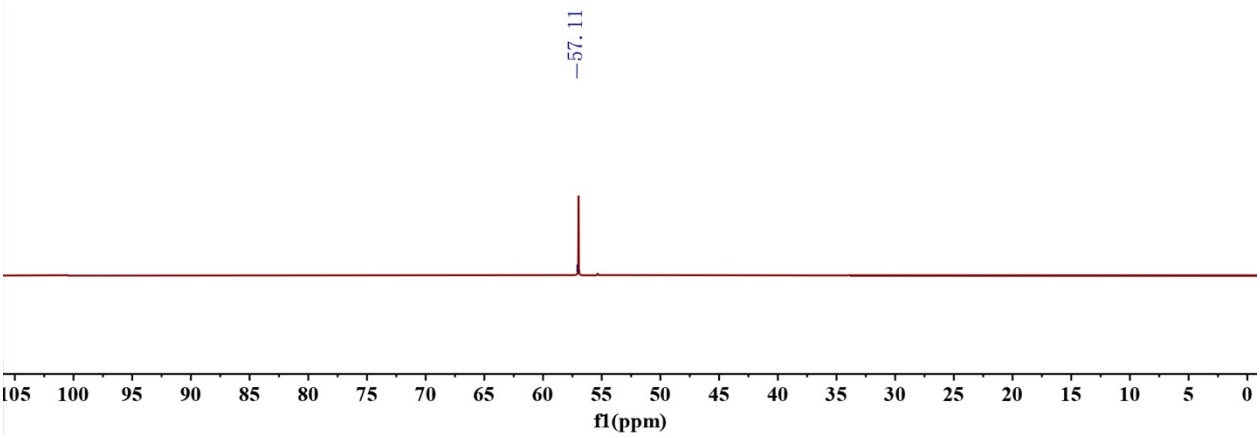

Figure S24. ^{31}P NMR (202 MHz, $CDCl_3$, ppm, 298 K) of **[Au_2Cl_2(*m*-P^P)]**.

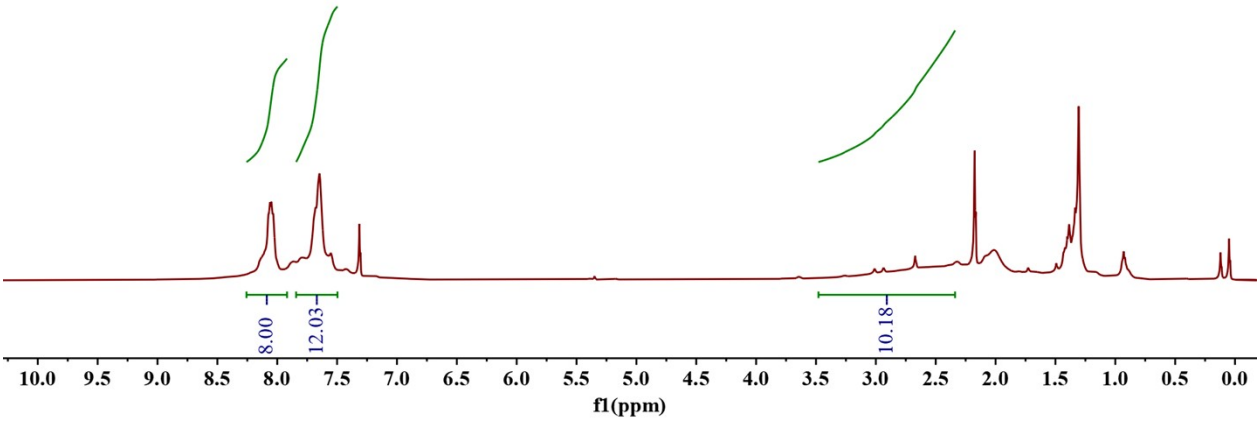

Figure S25. ^{1}H NMR (500 MHz, $CDCl_3$, ppm, 298 K) of **[$Au_2(BF_4)_2$(*m*-P^P)$_2$]** (with minor byproduct [Au_2(*m*-^{nido}P^P)$_2$]).

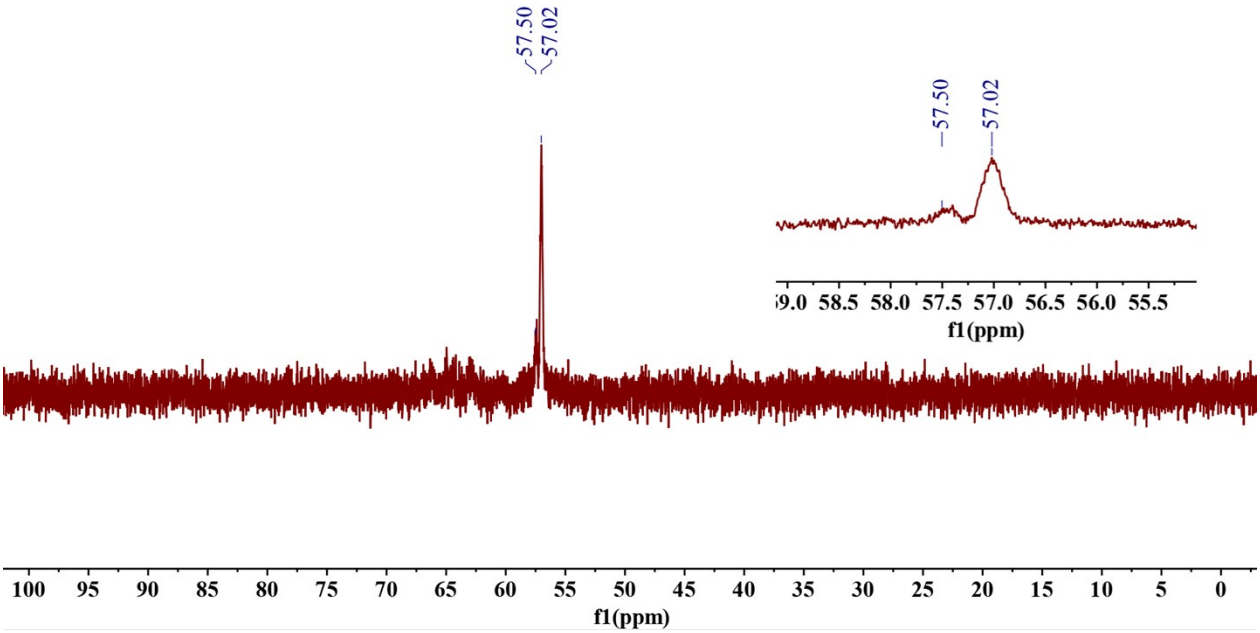

Figure S26. ^{31}P NMR (202 MHz, $CDCl_3$, ppm, 298 K) of $[Au_2(m\text{-P}\hat{}\text{P})_2][BF_4]_2$ (with minor byproduct $[Au_2(m\text{-}^{nido}\text{P}\hat{}\text{P})_2]$).

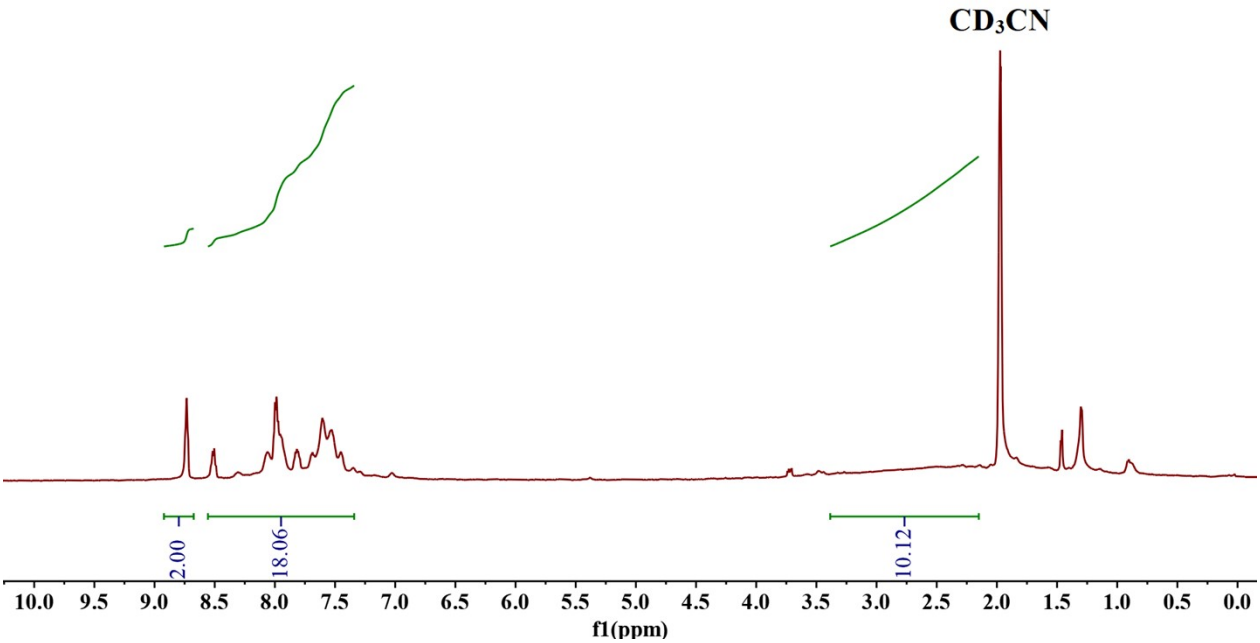

Figure S27. ^{1}H NMR (500 MHz, CD_3CN, ppm, 298 K) of **$[Au_{18}S_8(m\text{-P}\hat{}\text{P})_6][Cl_2]$**.

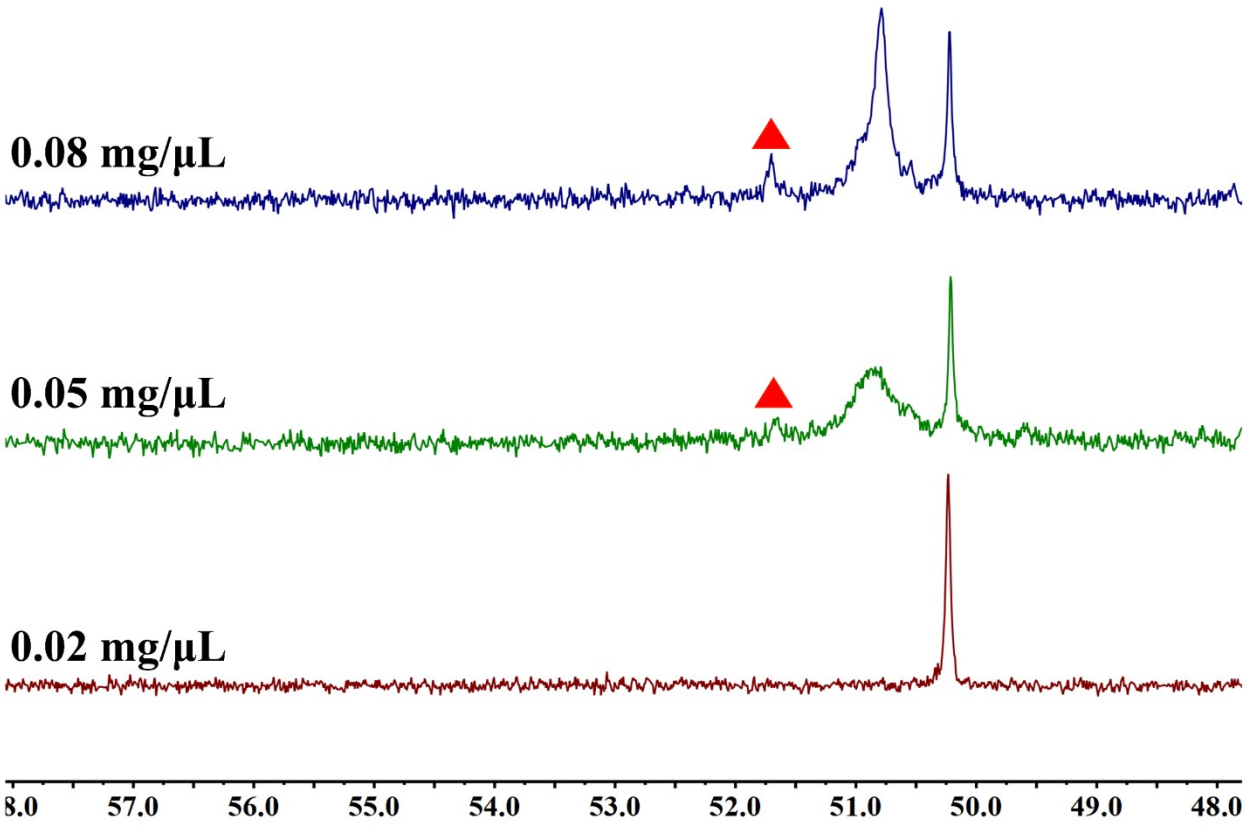

Figure S28. ^{31}P NMR (202 MHz, $CDCl_3$, ppm, 298 K) of **[$Au_{18}S_8$(*m*-P^P)$_6$][Cl_2]** with different concentrations.

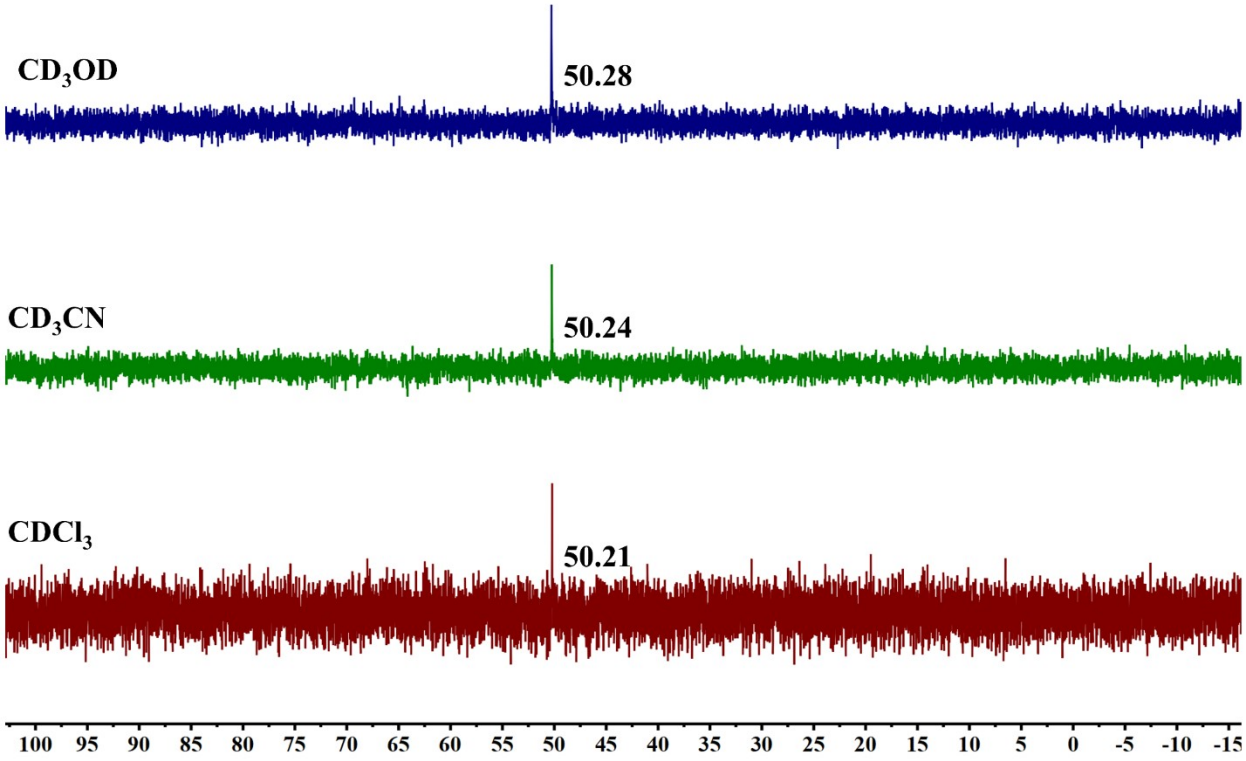

Figure S29. ^{31}P NMR (202 MHz, ppm, 298 K) of **[$Au_{18}S_8$(*m*-P^P)$_6$][Cl]$_2$** (~0.02 mg·μL) in different solvents.

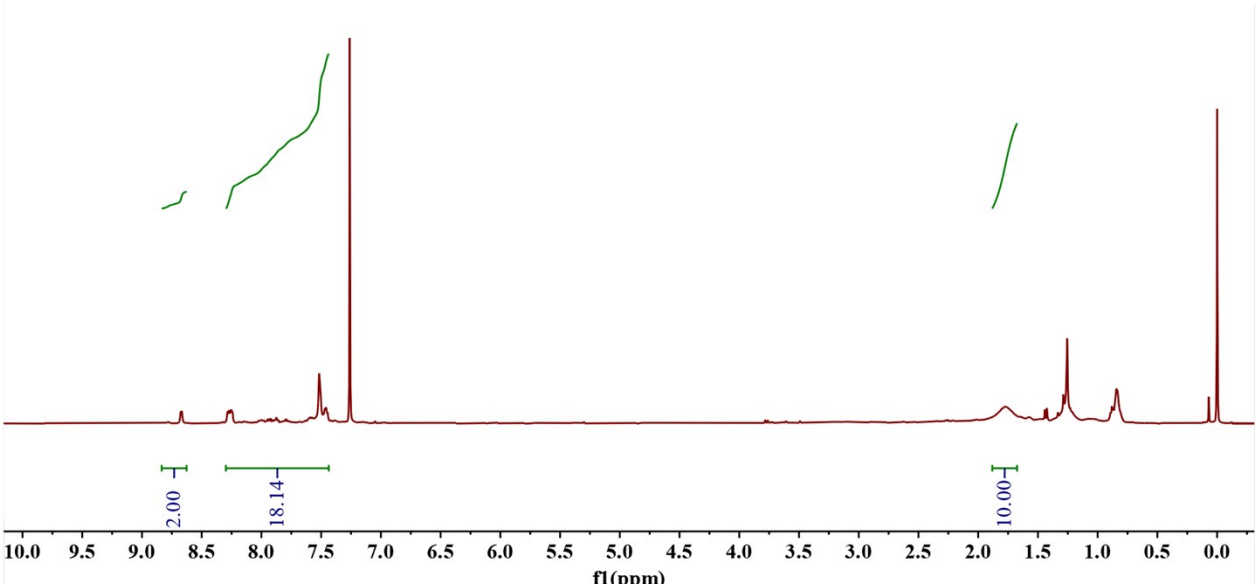

Figure S30. ^{1}H NMR (500 MHz, $CDCl_3$, ppm, 298 K) of [Au_8S_4(*m*-P^P)$_2$].

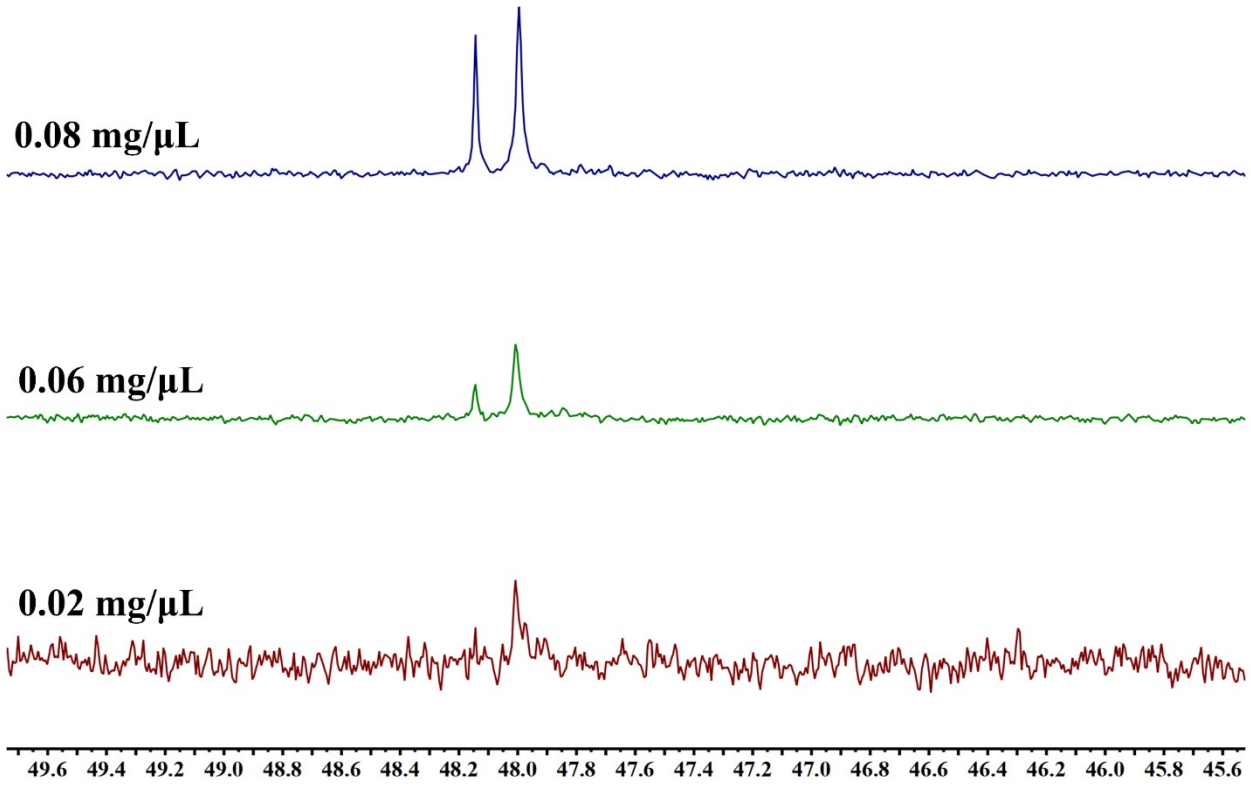

Figure S31. ^{31}P NMR (202 MHz, $CDCl_3$, ppm, 298 K) of $[Au_8S_4(m\text{-P}\hat{}\text{P})_2]$ with different concentrations.

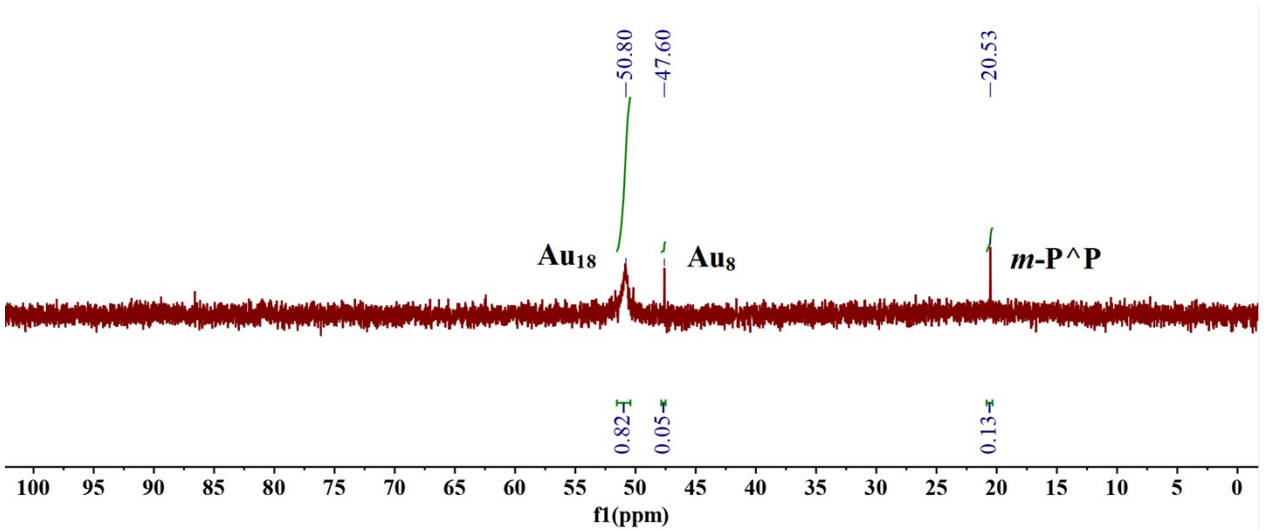

Figure S32. ^{31}P NMR (202 MHz, $CDCl_3$, ppm, 298 K) of pure $[Au_2Cl_2(m\text{-P}\hat{}\text{P})]$ reacting with H_2S without recrystallization (~0.02 mg/μL). The proportion of Au_{18}:Au_8 = 5.5:1.

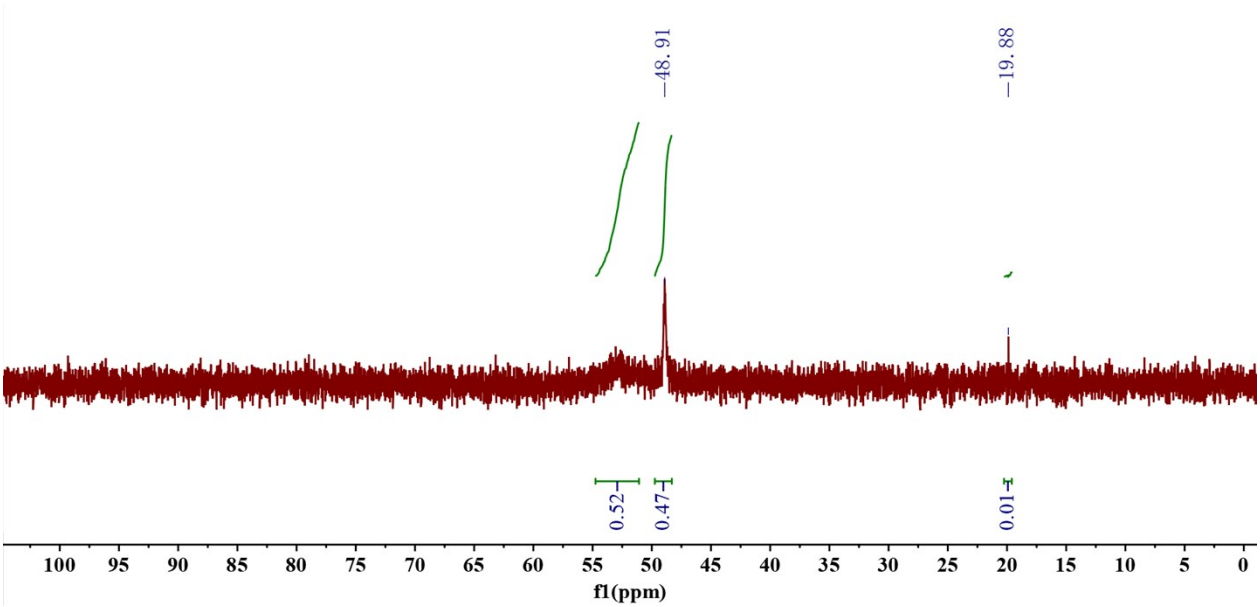

Figure S33. ^{31}P NMR (202 MHz, $CDCl_3$, ppm, 298 K) of pure [Au_2Cl_2(*m*-P^P)] reacting with Na_2S without recrystallization (~0.02 mg/μL). The proportion of Au_{18}:Au_8 = 1:2.7.

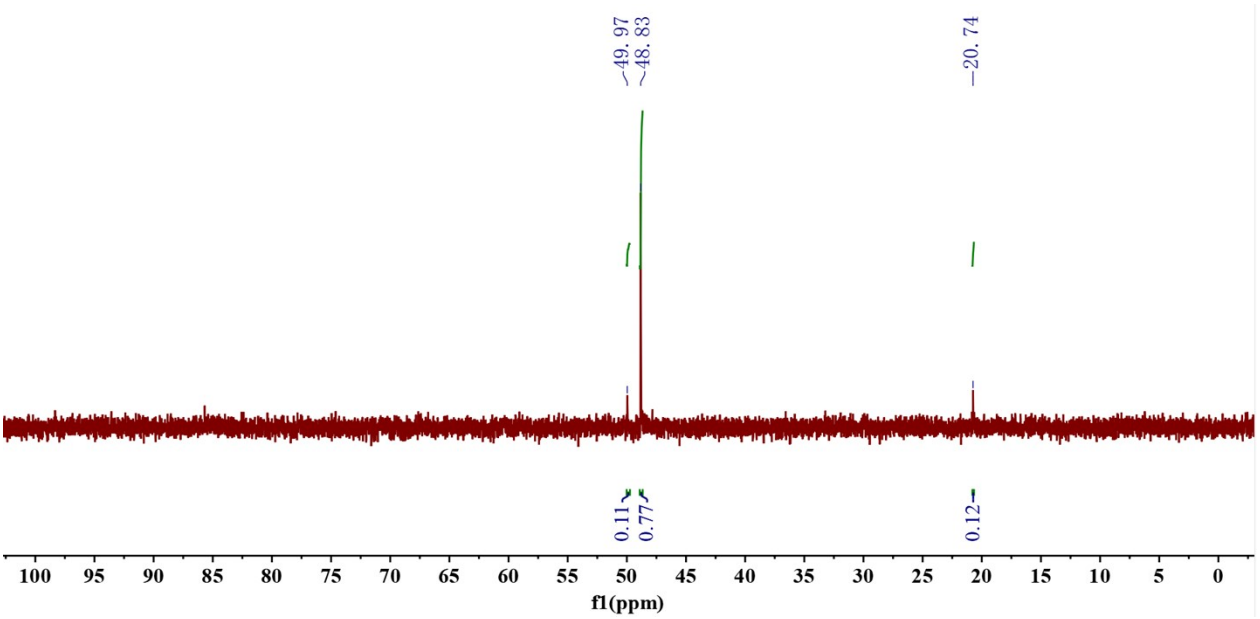

Figure S34. ^{31}P NMR (202 MHz, $CDCl_3$, ppm, 298 K) of pure [Au_2Cl_2(*m*-P^P)] reacting with $S(SiMe_3)_2$ without recrystallization (~0.02 mg/μL). The proportion of Au_{18}:Au_8 = 1:21.0.

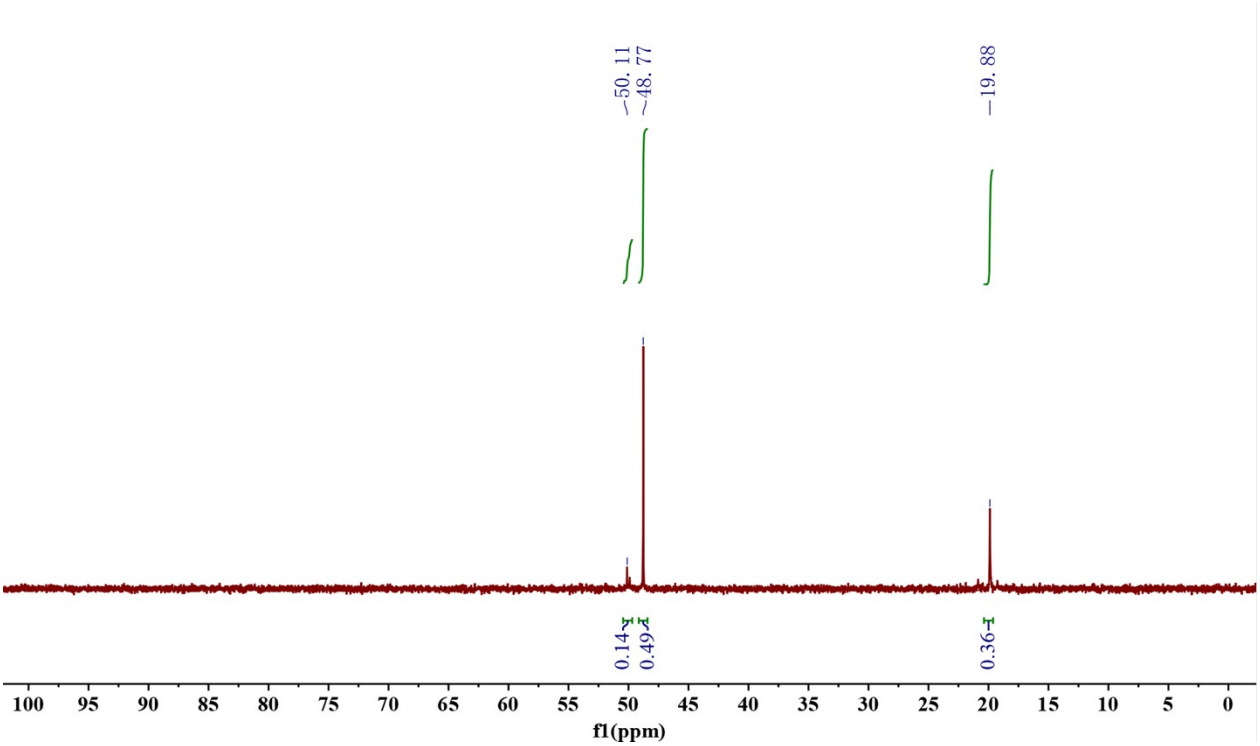

Figure S35. ^{31}P NMR (202 MHz, $CDCl_3$, ppm, 298 K) of pure $[Au_2(m\text{-P^P})_2][BF_4]_2$ reacting with H_2S without recrystallization (~0.02 mg/μL). The proportion of Au_{18}:Au_8 = 1:10.5.

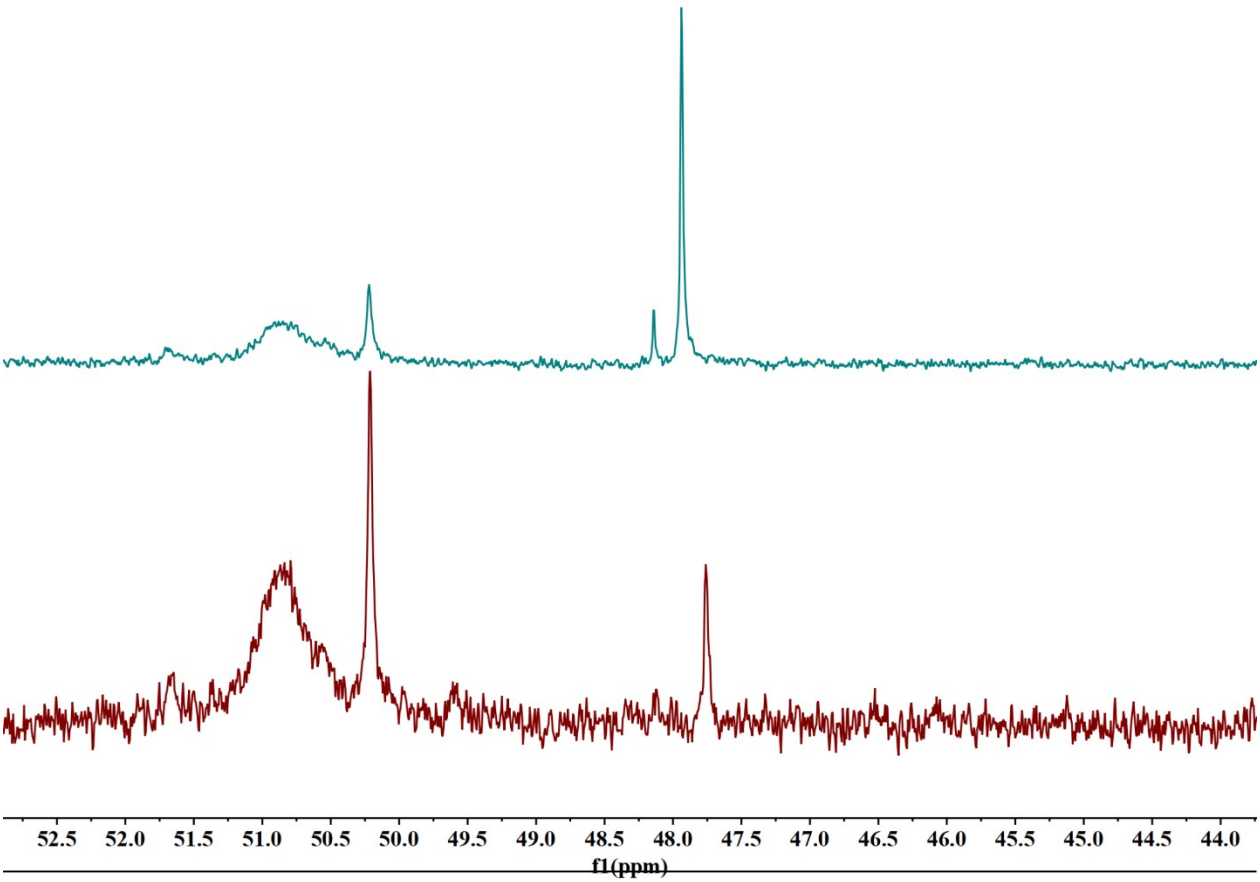

Figure S36. ^{31}P NMR (202 MHz, $CDCl_3$, ppm, 298 K) of pure [Au_2Cl_2(*m*-P^P)] reacting with H_2S and $S(SiMe_3)_2$ (above & below) without recrystallization (~0.06 mg/μL), respectively.

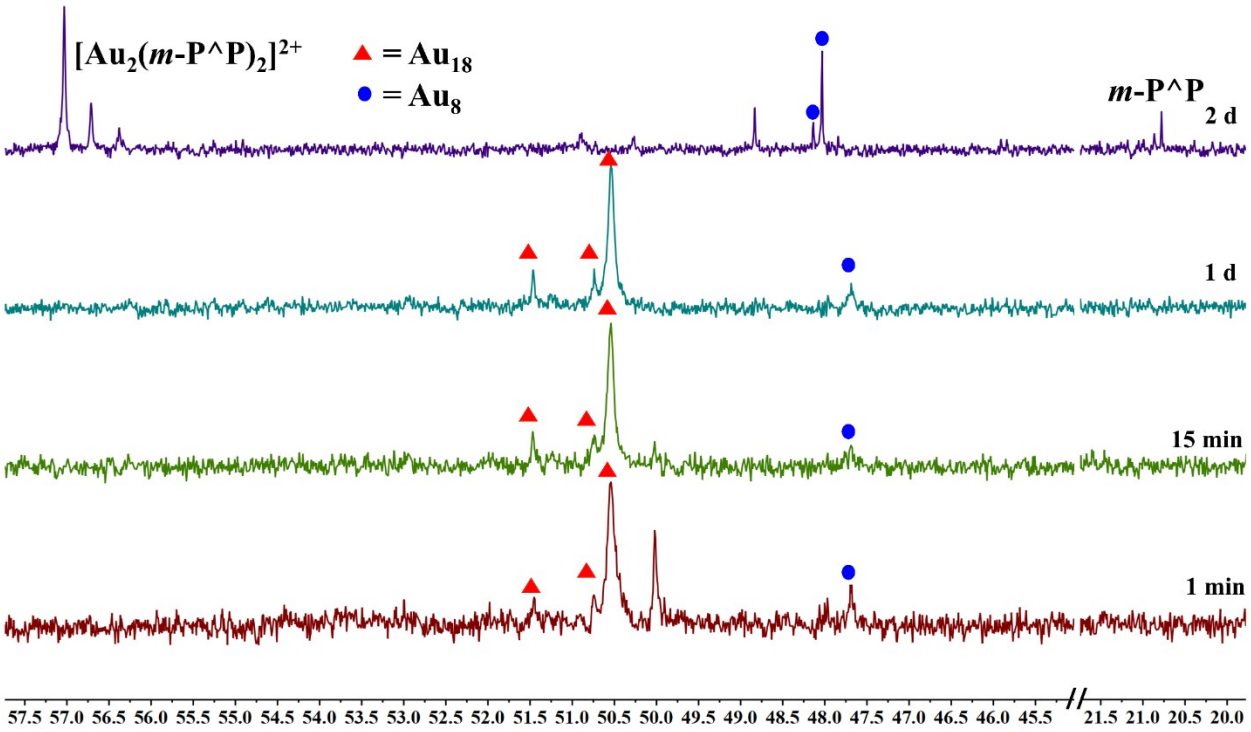

Figure S37. ^{31}P NMR spectrum of **Au_{18}** reacting with NH_4BF_4 at high concentration ($CDCl_3$: MeOH = 0.2 mL: 0.1 mL; **Au_{18}** = 15 mg, NH_4BF_4 = 5 mg).

Notes: A large amount of white precipitate appeared when introduced NH_4BF_4 (5 mg in 0.1mL MeOH) into **Au_{18}** solution, which may be the reason leading to the low conversion in one day (spectra **1 min~1 d**). A transient signal at 50.0 ppm in 1 min is likely attributable to interfacial heterogeneity between MeOH and $CDCl_3$, which gradually diminished as the system evolved toward interfacial energy minimization [7]. Subsequently, we took out of products from NMR tube into a round-bottom flask, 40 mL solution (DCM/MeOH = 1:1) was added and reacted for another one day. After solvent removal, pure $CDCl_3$ was selected to dissolve, leading to the nearly disappearance of **Au_{18}** signals (spectrum **2 d**).

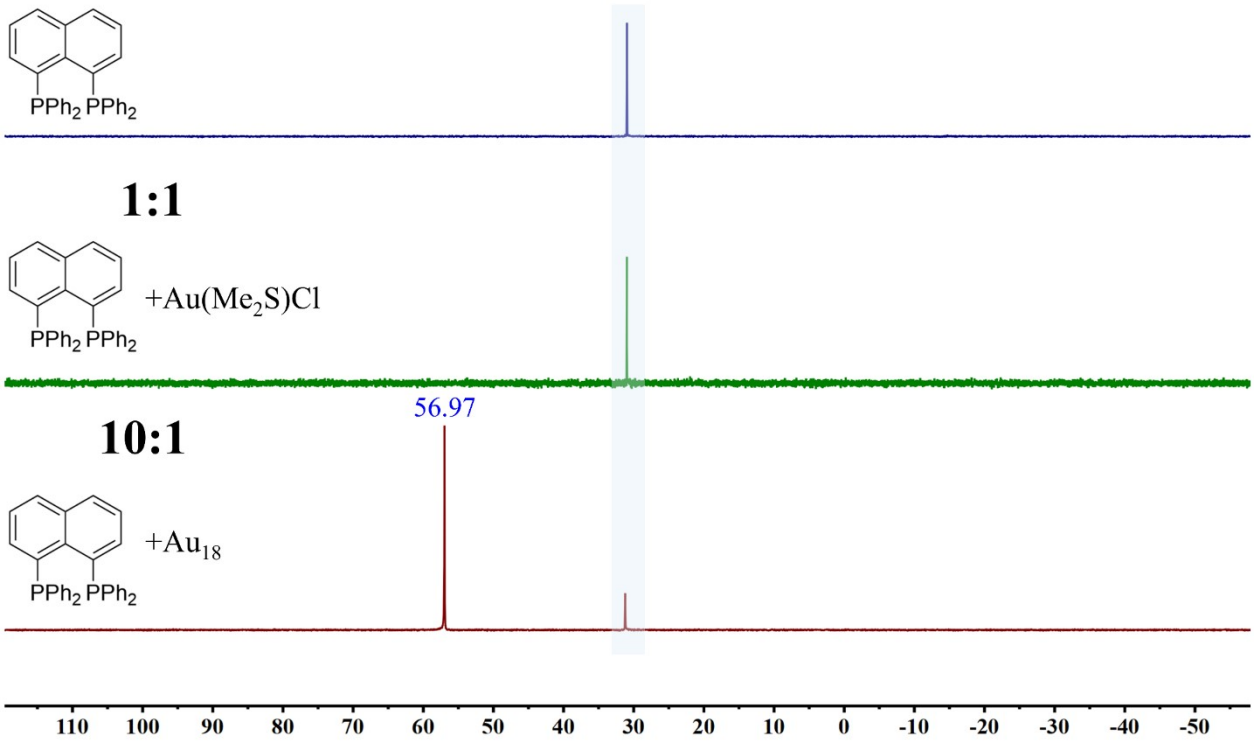

Figure S38. ^{31}P NMR (202 MHz, $CDCl_3$, ppm, 298 K) of $[Au_{18}S_8(m\text{-P^P})_6][Cl]_2$ reacting with Nap-P^P.

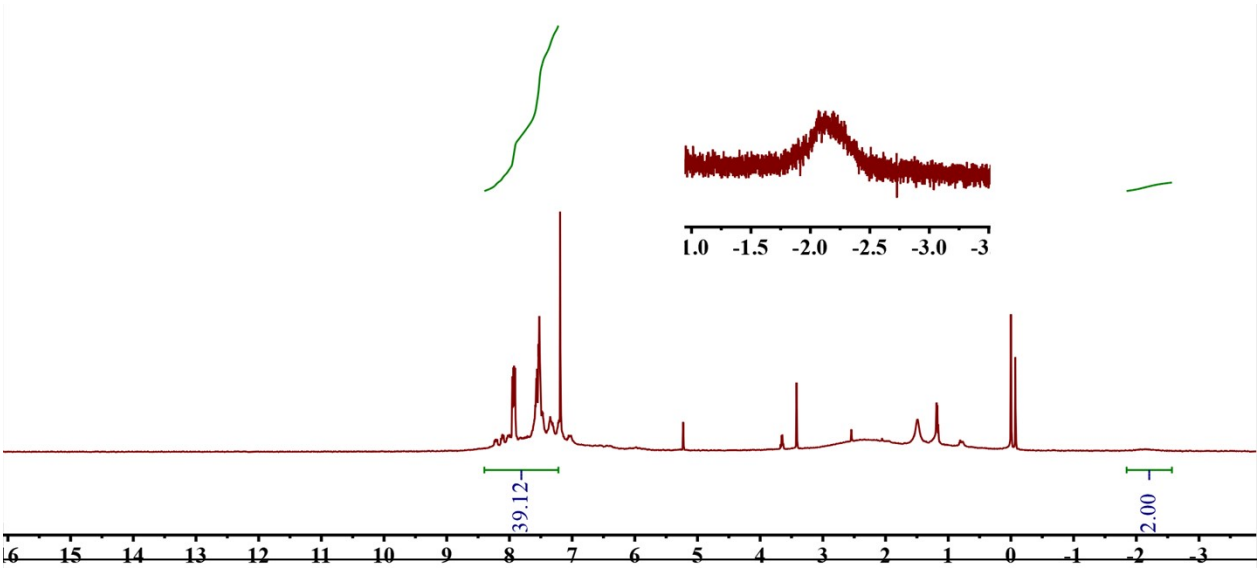

Figure S39. ^{1}H NMR (500 MHz, $CDCl_3$, ppm, 298 K) of $[Au_7(m\text{-P^P})_2(o\text{-}^{nido}P^P)_2]$.

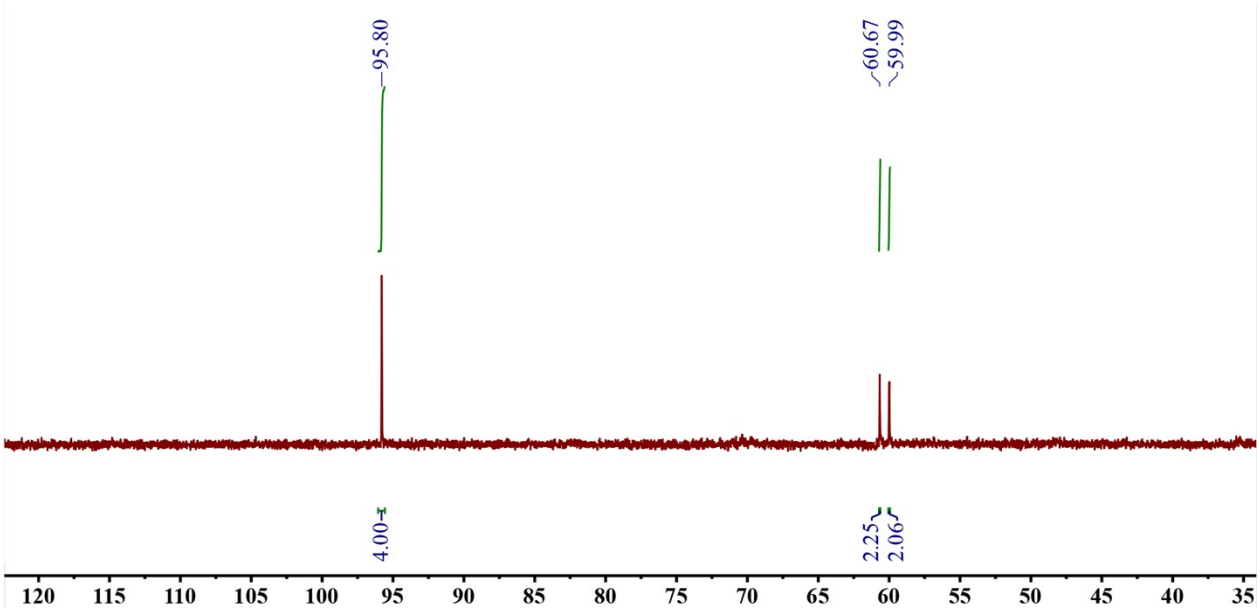

Figure S40. ^{31}P NMR (202 MHz, $CDCl_3$, ppm, 298 K) of $[Au_7(m\text{-P^P})_2(o\text{-}^{nido}P^P)_2]$.

4. Other data

$[Au_2(m\text{-}P\hat{}P)_2]^{2+}$

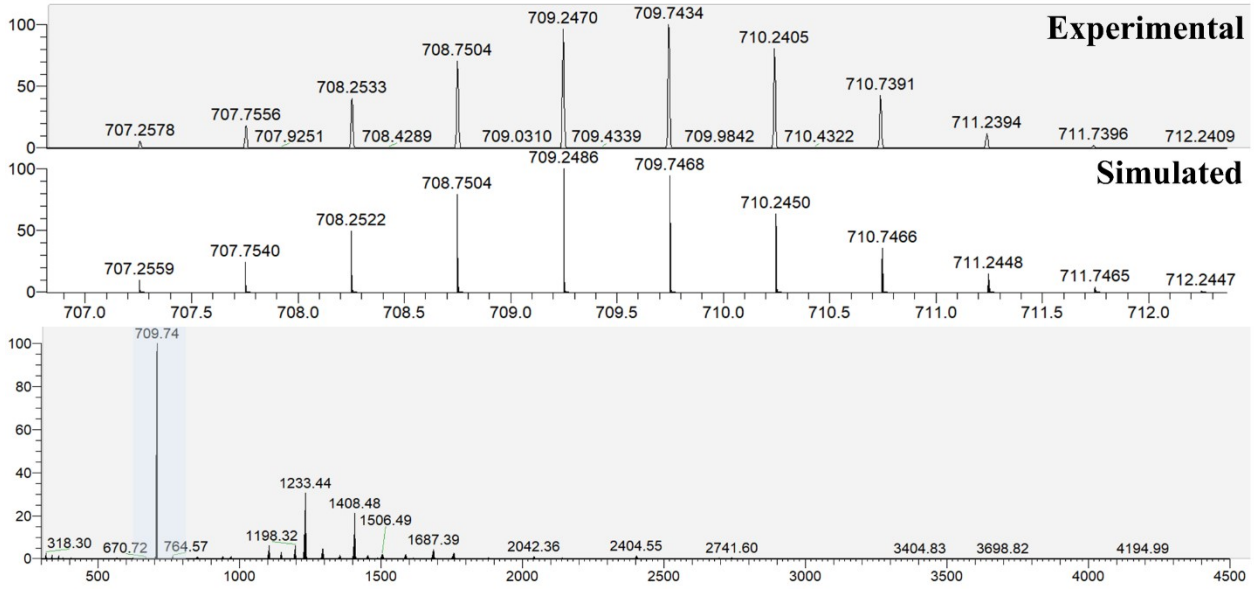

Figure S41. MALDI-TOF-MS spectrum of $[Au_2(m\text{-}P\hat{}P)_2]^{2+}$ ($[Au_2C_{52}H_{60}B_{20}P_4]^{2+}$) in CH_2Cl_2.

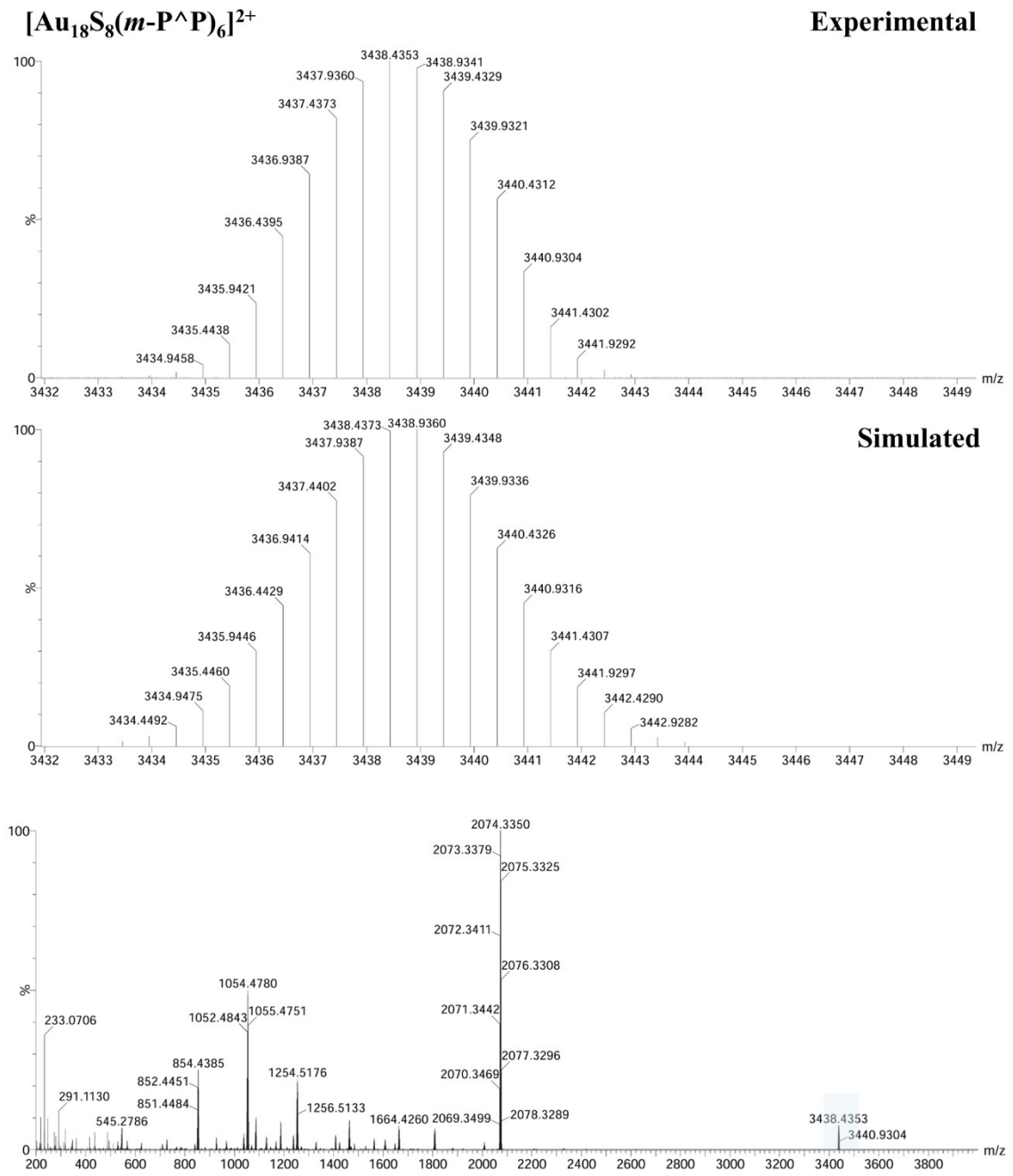

Figure S42. MALDI-TOF-MS spectrum of $[Au_{18}S_8(m\text{-P^P})_6][Cl]_2$ in $CDCl_3$.

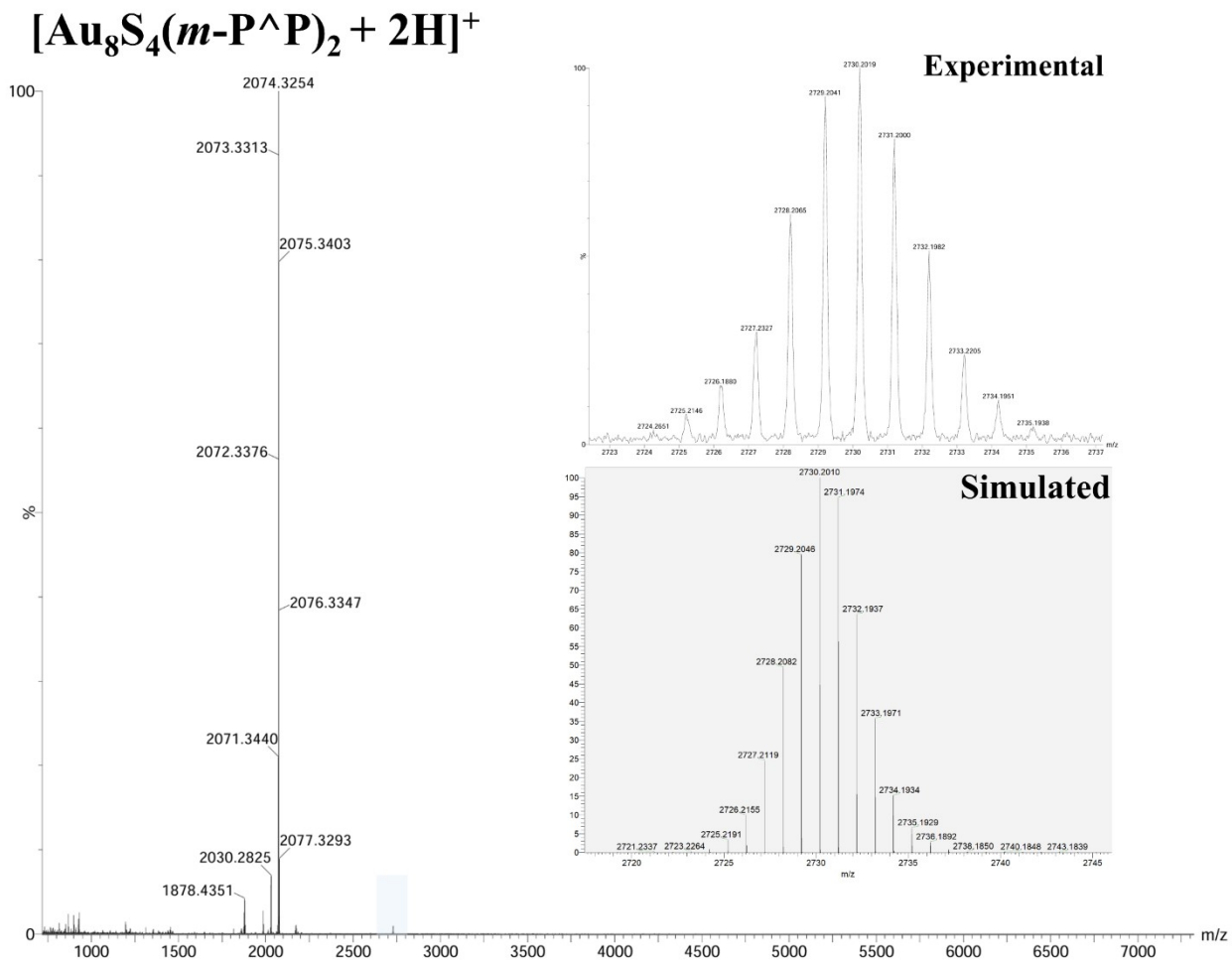

Figure S43. MALDI-TOF-MS spectrum of $[Au_8S_4(m\text{-P^P})_2]$in CH_2Cl_2.

Notes: A drop of HCOOH was added.

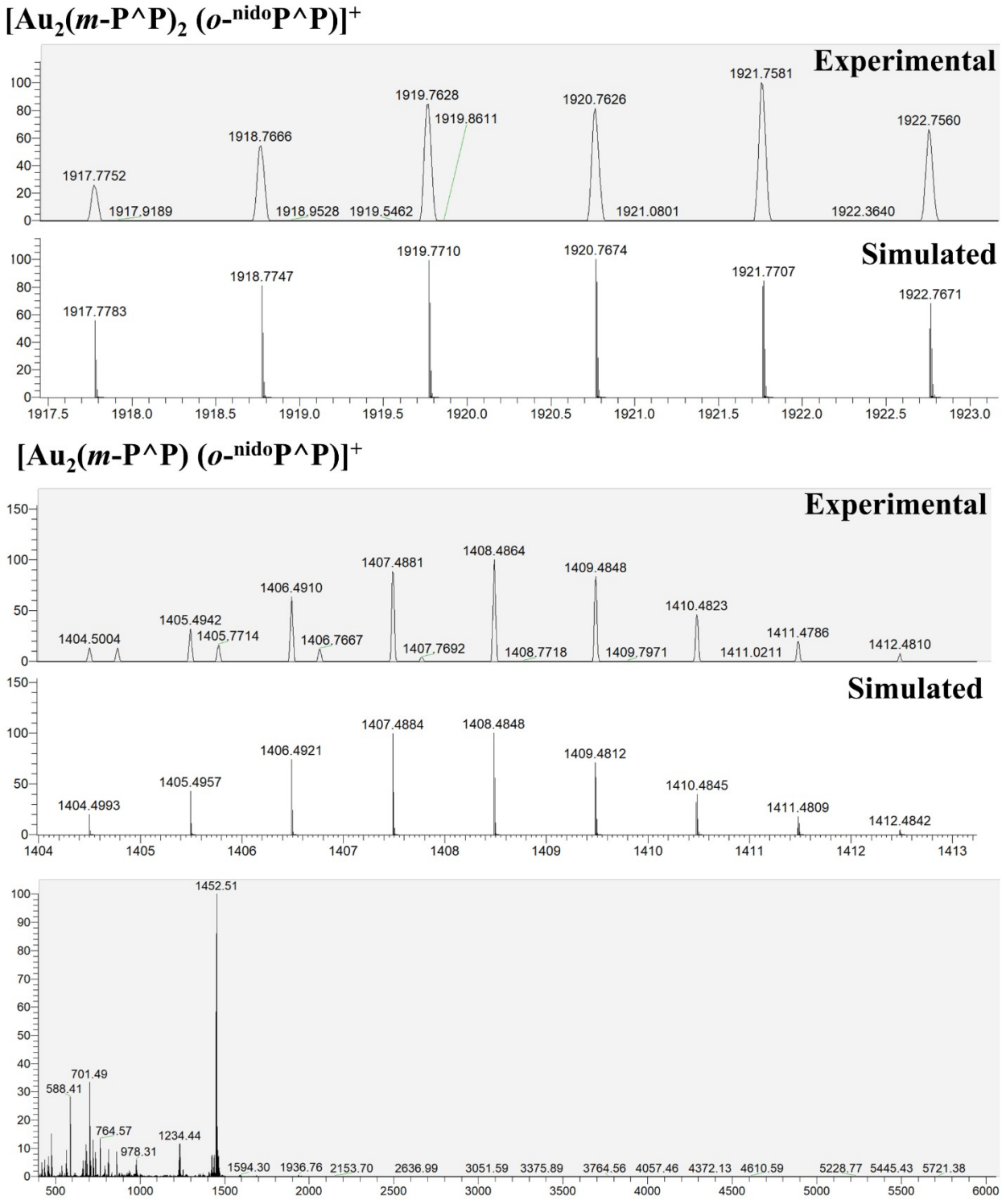

Figure S44. MALDI-TOF-MS spectrum of $[Au_7(m\text{-P}\hat{}\text{P})_2(o\text{-}^{nido}\text{P}\hat{}\text{P})_2]$ in CH_2Cl_2.

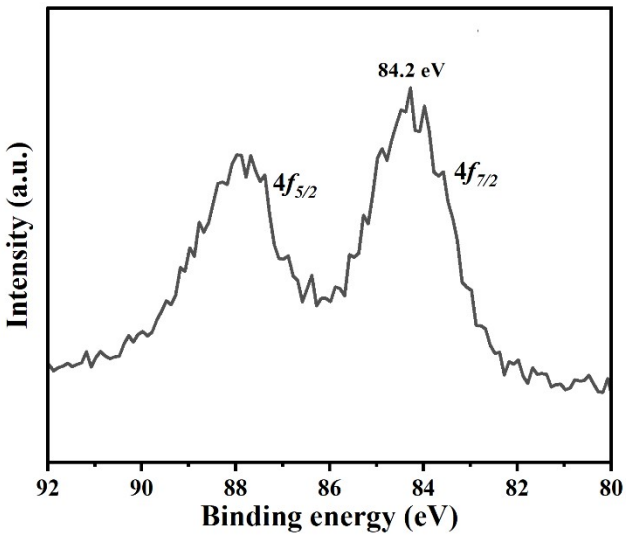

Figure S45. XPS spectrum of **Au_7**.

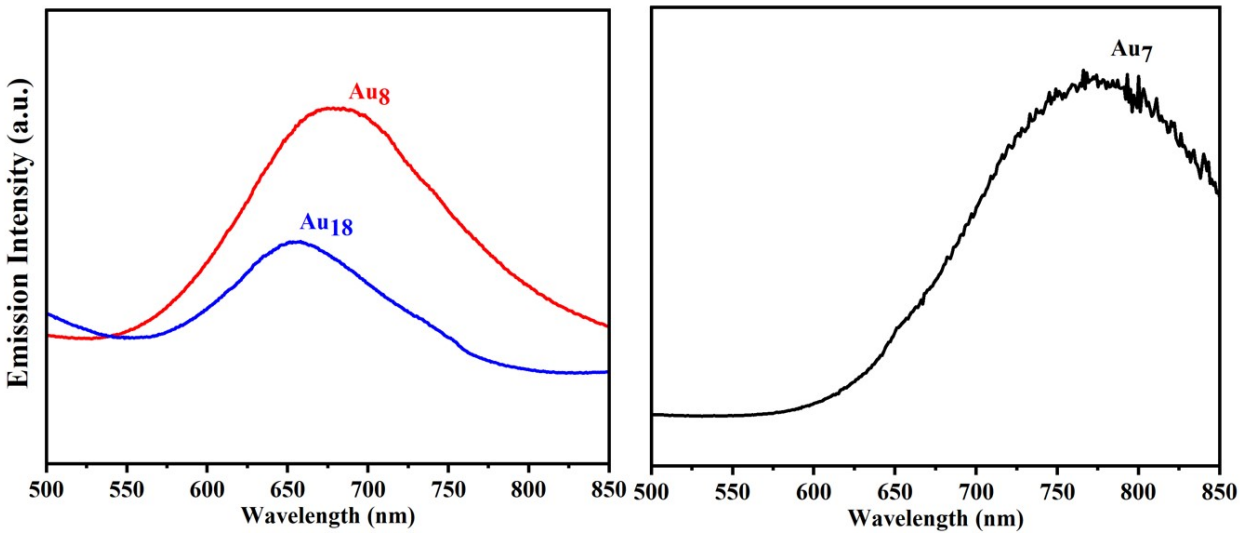

Figure S46. Solid-state emission spectra of clusters under 365 nm excitation at room temperature.

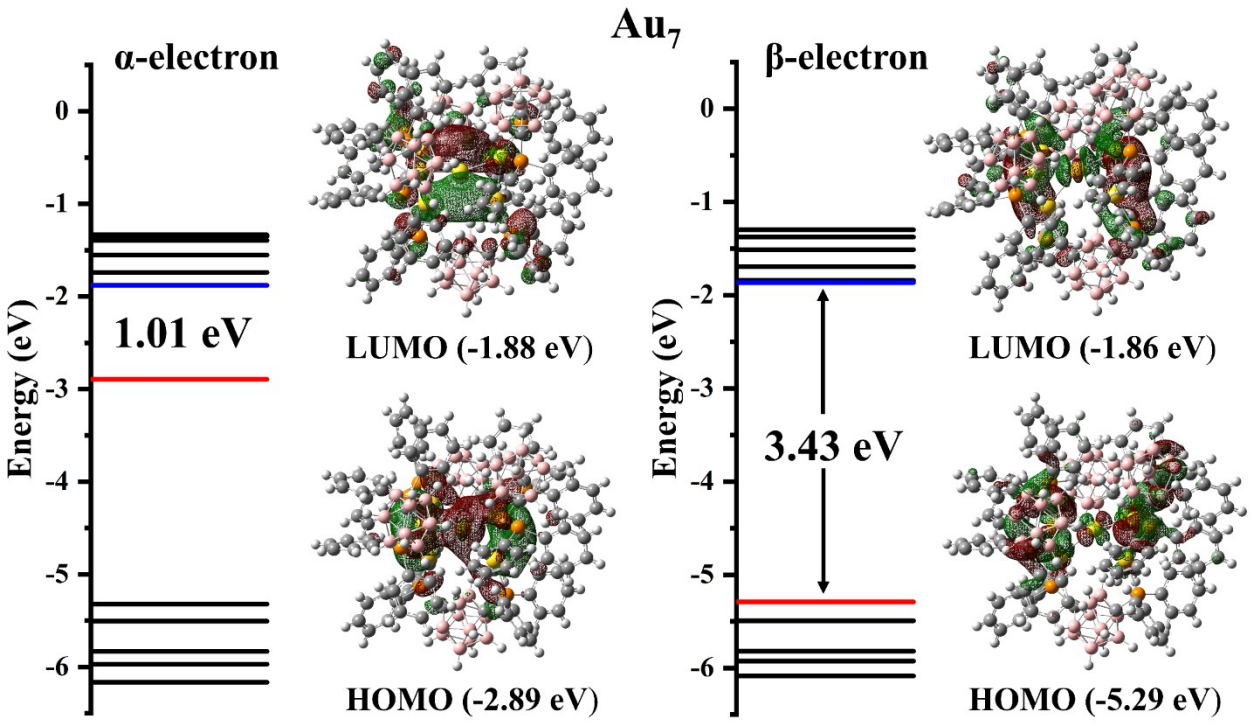

Figure S47. α- and β-electron orbits of **Au_7**.

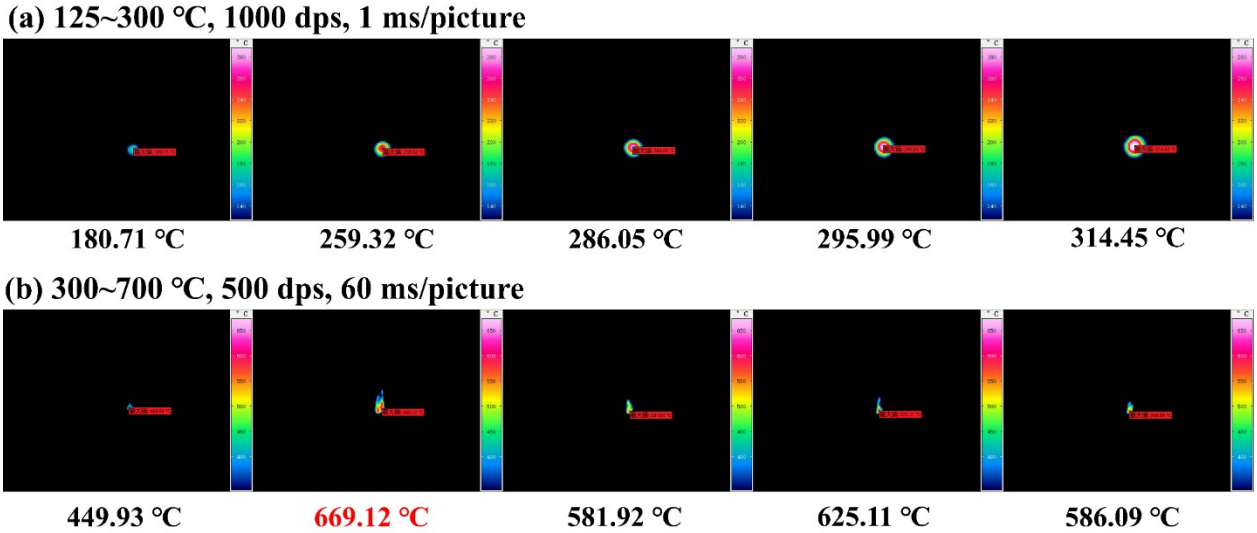

Figure S48. Flame temperature of **Au_7** recorded by a thermal infrared imager over two separate measurements.

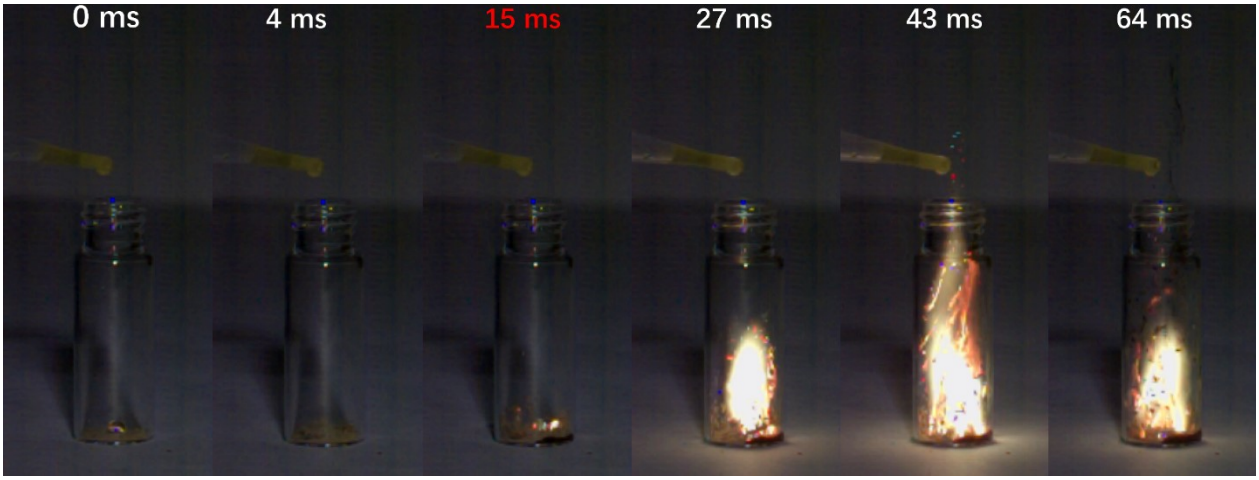

Figure S49. The second hypergolicity drop test of $\mathbf{Au_7}$.

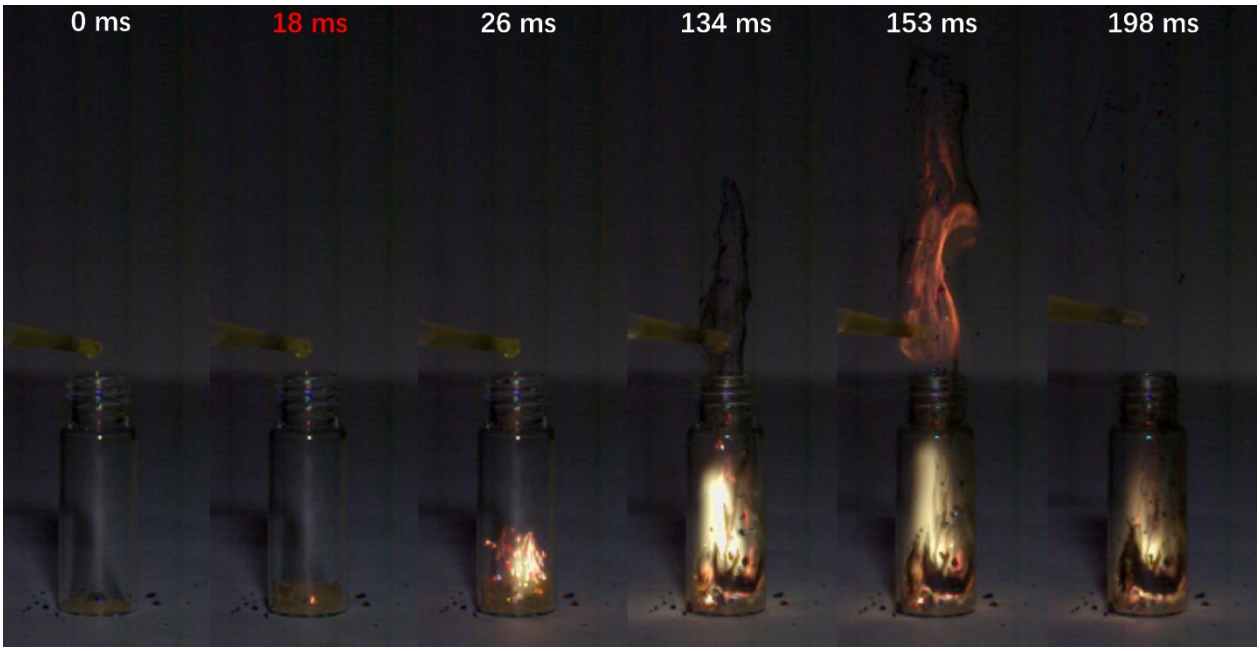

Figure S50. The third hypergolicity drop test of $\mathbf{Au_7}$.

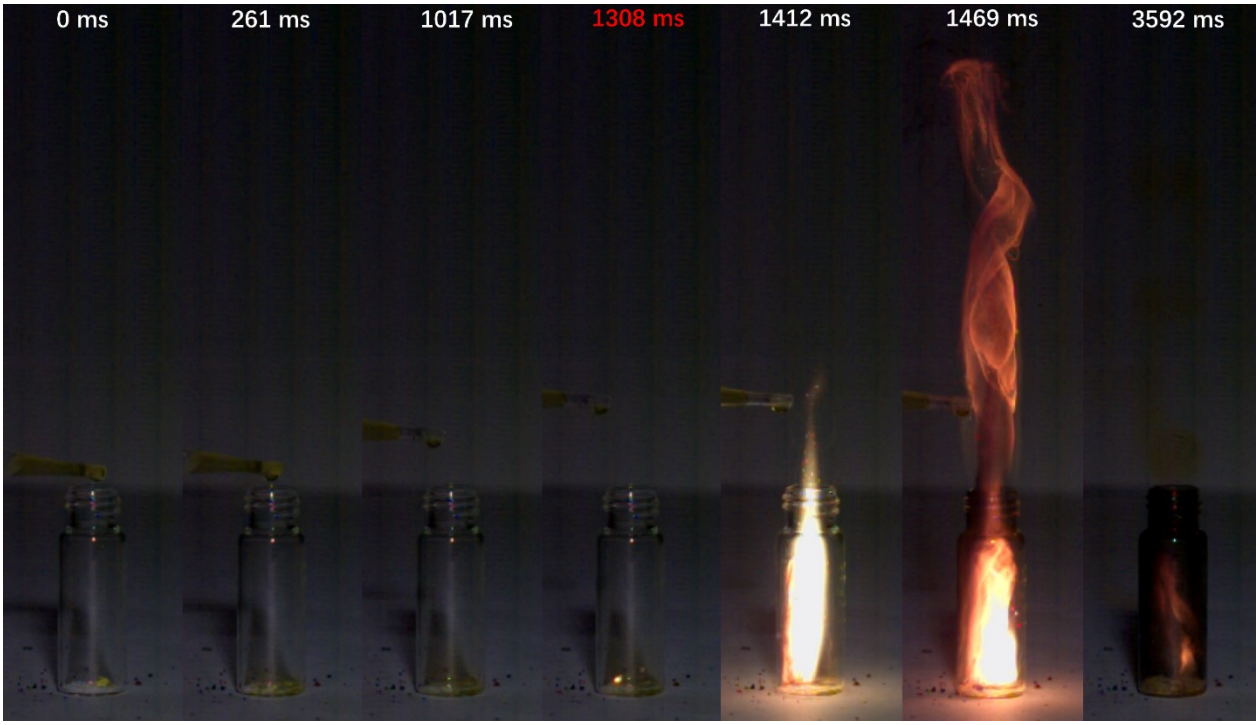

Figure S51. The successful hypergolicity drop test of *m*-P^P ligand. Full video is also provided.

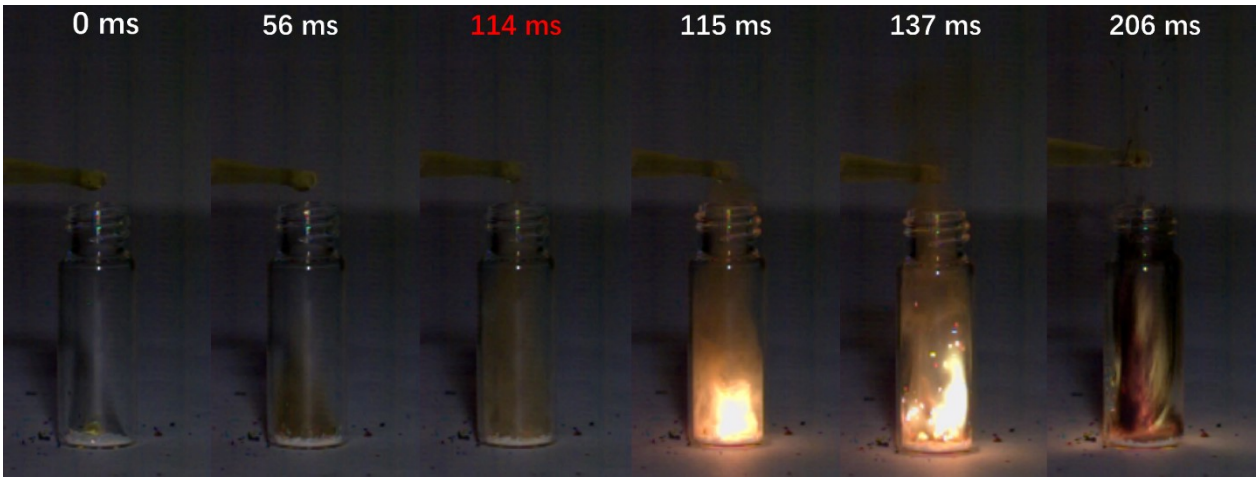

Figure S52. The successful hypergolicity drop test of *o*-P^P ligand. Full video is also provided.

Table S5. Energetic parameters of nanoclusters

Compounds	IS (J)[a]	FS (N)[b]	ID (ms)[c]	ΔH_c (kJ g^{-1})[d]
Au_{18} (This work)	>40	>360	× × ×	—
Au_8 (This work)	>40	>360	× × ×	—
Au_7 (This work)	>40	>360	14, 15, 18	23.5
Ag_{14} (Ref 8)	>40	>360	140	19.7
Cu_6Ag_8 (Ref 8)	>40	>360	15	23.5

[a] Impact Sensitivity, BAM standard;

[b] Friction Sensitivity, BAM standard;

[c] Ignited by WFNA for three times, × represents ignition failure;

[d] Heat of combustion, — represents no measurement due to the failure of ignited by WFNA. Test by oxygen bomb calorimetry, ~30 mg samples mixed with ~700 mg benzoic acid (-26434 ± 3 J·g^{-1}).

.

5. References

[1] Gaussian 16, Revision B.01, Frisch, M. J.; Trucks, G. W.; Schlegel, H. B.; Scuseria, G. E.; Robb, M. A.; Cheeseman, J. R.; Scalmani, G.; Barone, V.; Mennucci, B.; Petersson, G. A.; Nakatsuji, H.; Caricato, M.; Li, X.; Hratchian, H. P.; Izmaylov, A. F.; Bloino, J.; Zheng, G.; Sonnenberg, J. L.; Hada, M.; Ehara, M.; Toyota, K.; Fukuda, R.; Hasegawa, J.; Ishida, M.; Nakajima, T.; Honda, Y.; Kitao, O.; Nakai, H.; Vreven, T.; Montgomery, J. A., Jr.; Peralta, J. E.; Ogliaro, F.; Bearpark, M.; Heyd, J. J.; Brothers, E.; Kudin, K. N.; Staroverov, V. N.; Kobayashi, R.; Normand, J.; Raghavachari, K.; Rendell, A.; Burant, J. C.; Iyengar, S. S.; Tomasi, J.; Cossi, M.; Rega, N.; Millam, J. M.; Klene, M.; Knox, J. E.; Cross, J. B.; Bakken, V.; Adamo, C.; Jaramillo, J.; Gomperts, R.; Stratmann, R. E.; Yazyev, O.; Austin, A. J.; Cammi, R.; Pomelli, C.; Ochterski, J. W.; Martin, R. L.; Morokuma, K.; Zakrzewski, V. G.; Voth, G. A.; Salvador, P.; Dannenberg, J. J.; Dapprich, S.; Daniels, A. D.; Farkas, Ö.; Foresman, J. B.; Ortiz, J. V.; Cioslowski, J.; Fox, D. J. Gaussian, Inc., Wallingford CT, 2016.

[2] GaussView, Version 6, Gaussian, Inc., Wallingford CT.

[3] R.P. Alexander and H. Schroeder, Chemistry of Decaborane-Phosphorus Compounds. VI. Phosphino-*m*-carboranes, *Inorg. Chem.*, **1966**, *5*, 493–495.

[4] J. A. Ioppolo, J. K. Cleggb and L. M. Rendina, Dicarba-closo-dodecaborane(12) derivatives of phosphonium salts: easy formation of *nido*-carborane phosphonium zwitterions, *Dalton Trans.*, **2007**, 1982–1985.

[5] L.J. Bourhis, O.V. Dolomanov, R.J. Gildea, J.A.K. Howard, and H. Puschmann, The anatomy of a comprehensive constrained, restrained refinement program for the modern computing environment - Olex2 dissected, *Acta Cryst. A*, **2015**, 71, 59–75.

[6] G.M. Sheldrick, Crystal structure refinement with SHELXL, *Acta Cryst. C*, 2015, 71, 3–8.

[7] Duary, S.; Jana, A.; Das, A.; Sharma, A.; Pathak, B.; Adarsh, K.; Pradeep, T. Solvent-Modulated Luminescent Spheroidal Assemblies of Cu_8 Nanocluster for Volatile Amine Sensing. *Inorg. Chem.* **2025**, *64* (22), 11001–11011.

[8] Wang, Q. Y.; Wang, J.; Wang, S.; Wang, Z. .Y.; Cao, M.; He, C. L.; Yang, J. Q.; Zang, S. Q.; Thomas, C. W. M. *o*-Carborane-Based and Atomically Precise Metal Clusters as Hypergolic Materials. *J. Am. Chem. Soc.* **2020**, *142*, 12010−12014.